Monthly Notices of the ROYAL ASTRONOMICAL SOCIETY

MNRAS **529,** 3563–3581 (2024) https://doi.org/10.1093/mnras/stae651
Advance Access publication 2024 March 5

Exploring the nature of UV-bright $z \gtrsim 10$ galaxies detected by *JWST*: star formation, black hole accretion, or a non-universal IMF?

Alessandro Trinca [1,2,3★] Raffaella Schneider [1,2,3,4] Rosa Valiante [1,3] Luca Graziani,[2,3] Arianna Ferrotti,[2] Kazuyuki Omukai[5] and Sunmyon Chon [5,6]

[1]*INAF/Osservatorio Astronomico di Roma, Via Frascati 33, I-00040 Monte Porzio Catone, Italy*
[2]*Dipartimento di Fisica, 'Sapienza' Universitàdi Roma, Piazzale Aldo Moro 2, I-00185 Roma, Italy*
[3]*Dipartimento di Fisica, INFN, Sezione Roma1, 'Sapienza' Universitàdi Roma, Piazzale Aldo Moro 2, I-00185 Roma, Italy*
[4]*Sapienza School for Advanced Studies, Viale Regina Elena 291, I-00161 Roma, Italy*
[5]*Astronomical Institute, Graduate School of Science, Tohoku University, Aoba, Sendai 980-8578, Japan*
[6]*Max-Planck-Institut für Astrophysik, Karl-Schwarzschild-Str. 1, D-85741 Garching, Germany*

Accepted 2024 February 28. Received 2024 February 12; in original form 2023 May 8

ABSTRACT

We use the Cosmic Archaeology Tool (CAT) semi-analytical model to explore the contribution of Population (Pop) III/II stars and active galactic nuclei (AGNs) to the galaxy ultraviolet (UV) luminosity function (LF) evolution at $4 \leq z \leq 20$. We compare in particular with recent *JWST* data in order to explore the apparent tension between observations and theoretical models in the number density of bright galaxies at $z \gtrsim 10$. The model predicts a star formation history dominated by UV faint ($M_{\rm UV} > -18$) galaxies, with a Pop III contribution of $\lesssim 10$ per cent ($\lesssim 0.5$ per cent) at $z \simeq 20$ ($z \simeq 10$). Stars are the primary sources of cosmic reionization, with 5 per cent–10 per cent of ionizing photons escaping into the intergalatic medium at $5 \leq z \leq 10$, while the contribution of unobscured AGNs becomes dominant only at $z \lesssim 5$. The predicted stellar and AGN UV LFs reproduce the observational data at $5 \lesssim z \lesssim 9$–10. At higher redshift, CAT predicts a steeper evolution in the faint-end slope ($M_{\rm UV} > -18$), and a number density of bright galaxies ($M_{\rm UV} \simeq -20$) consistent with data at $z \sim 10$–11, but smaller by 0.8 dex at $z \sim 12$–13, and 1.2 dex at $z \sim 14$–16, when compared to the values estimated by recent studies. Including the AGN emission does not affect the above findings, as AGNs contribute at most to $\lesssim 10$ per cent of the total UV luminosity at $M_{\rm UV} < -19$ and $z \gtrsim 10$. Interestingly, considering a gradual transition in the stellar initial mass function, modulated by metallicity and redshift as suggested by recent simulations, the model agrees with *JWST* data at $z \sim 12$–13, and the disagreement at $z \sim 14$–16 is reduced to 0.5 dex.

Key words: galaxies: active – galaxies: high-redshift – galaxies: luminosity function, mass function – quasars: supermassive black holes – dark ages, reionization, first stars – cosmology: theory.

1 INTRODUCTION

The launch of *JWST* represents a major breakthrough in our understanding of the high-redshift Universe. The early release observations enabled the detection of several galaxy candidates with photometric redshifts $z \gtrsim 10$ (Bradley et al. 2023; Castellano et al. 2022; Labbe et al. 2023; Naidu et al. 2022; Tacchella et al. 2023a, b; Atek et al. 2023; Donnan et al. 2023; Williams et al. 2023; Adams et al. 2023b; Harikane et al. 2023b), some of which with spectroscopic confirmation (Schaerer et al. 2022; Wang et al. 2022; Heintz et al. 2023a, b; Arrabal Haro et al. 2023; Bunker et al. 2023; Curti et al. 2023; Harikane et al. 2024), including the currently most distant galaxy at $z = 13.2$ (Curtis-Lake et al. 2023). This provides an unprecedented opportunity to explore the properties of the galaxy population in the first few hundreds million years of cosmic history, and to constrain their evolution. In particular, deep *JWST* observations are starting to constrain the low-mass end of the black hole (BH) mass function at $z \sim 4$–7 (Kocevski et al. 2023; Übler et al. 2023; Harikane et al. 2023a; Maiolino et al. 2023c), observe accreting supermassive black holes (SMBHs) in the nuclei of galaxies at $z \sim 9$–11 (Larson et al. 2023; Maiolino et al. 2023a), and detect potential signatures of the first stellar populations (Wang et al. 2022; Welch et al. 2022; Vanzella et al. 2023; Maiolino et al. 2023b).

The wealth of early *JWST* observations is already starting to challenge theoretical models. In particular, the number density of bright galaxies and its apparent lack of evolution between $z \sim 9$ and $\sim$ 13–17 are in tension with standard model predictions (Finkelstein et al. 2023). Several physical causes have already been proposed to relieve this tension. A first possibility is that the observed ultraviolet (UV) bright galaxies arise as outliers of the general population, due to variations in halo formation histories, which lead to young ages ($\sim$10 Myr) and high star formation rates (SFRs, Mason, Trenti & Treu 2023). Alternatively, the observed UV luminosity function (LF) at $z \gtrsim 10$ can be reproduced if the interstellar dust is evacuated by radiatively driven outflows during the earliest phase of galaxy build-up (Ferrara, Pallottini & Dayal 2023; Fiore et al. 2023; Ziparo et al. 2023). An overabundance of bright objects could

★ E-mail: alessandro.trinca@inaf.it

also be explained if galaxies produce stars or UV photons more efficiently than expected due to a lack of SF suppression at pre-reionization epochs (Harikane et al. 2023b), feedback-free starbursts (Dekel et al. 2023), less efficient stellar-driven winds (Yung et al. 2024), or to a more top-heavy stellar initial mass function (IMF) characterizing stellar populations at high redshift (Inayoshi et al. 2022; Finkelstein et al. 2023; Yung et al. 2024; Harikane et al. 2023b, 2024). Indeed, the fraction of massive stars in high-redshift stellar populations is expected to increase as a result of both the low metallicity (Omukai et al. 2005; Hirano et al. 2014, 2015; Chon, Hosokawa & Omukai 2021) and the higher temperature of the cosmic microwave background (CMB, Schneider & Omukai 2010; Chon et al. 2022). A considerable evolution of the stellar IMF might therefore be expected at $z \gtrsim 10$, resulting into a reduced mass-to-light ratio in early galaxies. To test this hypothesis, spectroscopic signatures associated to the presence of massive stars, such as strong nebular line emission and significant SN-driven galactic winds, will be tested by forthcoming observations (Katz et al. 2023; Nakajima & Maiolino 2022; Trussler et al. 2023). By looking at the inferred properties of *JWST* photometric sources (stellar masses, ages, and UV slopes), Mirocha & Furlanetto (2023) argue that a combination of increased SF efficiency, short-term temporal variations in the SFR, and dust attenuation is required to match the observations. When the comparison is made with spectroscopically confirmed sources (Curtis-Lake et al. 2023; Arrabal Haro et al. 2023; Robertson et al. 2023), Keller et al. (2023) and McCaffrey et al. (2023) show that that existing cosmological simulations with varying resolution can generally reproduce the observations in terms of galaxy stellar masses, SFRs, and number density of galaxies at $z > 10$. Similarly, Prada et al. (2023) show that forecasts of a standard cosmological galaxy formation model[1] are consistent with the abundance of photometrically selected *JWST*/*Hubble Space Telescope* (*HST*) galaxies at $z = 8$, 9, and 10, and with the properties of spectroscopically confirmed galaxies at the same redshift; an exception is represented by the sample of red massive photometrically selected galaxies identified by Labbe et al. (2023) at $z \sim 8$, whose stellar masses exceeding $10^{10}\,\mathrm{M}_\odot$ may be affected by systematic errors, but if real would require a revision of the standard galaxy formation model (see e.g. Menci et al. 2022).

The above quoted studies show the complexity of interpreting early *JWST* measurements. One additional possibility is that at least a fraction of the observed UV luminosity densities at $z \gtrsim 10$ are produced by active galactic nucleus (AGN) activity (Pacucci et al. 2022). Indeed, ongoing *JWST* surveys, such as JADES Medium/Deep, CEERS, and PRIMER, are expected to be sensitive enough to detect tens of accreting BHs with masses $M_{\rm BH} = 10^6$–$10^8\,\mathrm{M}_\odot$ at $7 \leq z \leq 10$, with JADES Deep having the sensitivity to detect growing BHs with masses $M_{\rm BH} = 10^4$–$10^6\,\mathrm{M}_\odot$ at $z \gtrsim 10$ (Trinca et al. 2023). While most of the $z \sim 12$–16 *JWST* candidates show extended morphologies (Harikane et al. 2023b), *JWST* NIRSpec spectroscopy have detected broad emission lines from low-luminosity AGNs at $z \sim 4$–7 (Kocevski et al. 2023; Übler et al. 2023; Harikane et al. 2023a; Maiolino et al. 2023c) and from sources at $z = 9$–11 (Larson et al. 2023; Maiolino et al. 2023a), suggesting that AGN activity may contribute to the UV luminosity of at least a fraction of these sources. The estimated BH masses are $\sim 10^7$–$10^8\,\mathrm{M}_\odot$ and the $M_{\rm BH}/\mathrm{M}_*$ ratio is higher than the empirical relationship measured for nearby broad-line AGNs with comparable BH masses (Reines & Volonteri 2015).

[1]They combine Uchuu *N*-body simulations (Ishiyama et al. 2021) with the Universe Machine galaxy formation algorithm (Behroozi et al. 2019).

These findings are consistent with the expectations of theoretical models (Schneider et al. 2023), which show that *JWST* surveys have the sensitivity to detect early accreting BHs out to $z \sim 10$ (Trinca et al. 2023), provided that these systems are overmassive with respect to their host galaxy stellar mass (Volonteri, Habouzit & Colpi 2023). Interestingly, none of the systems is detected in X-rays, and their position on the BPT (Baldwin, Phillips & Terlevich 1981), or the OHNO (Backhaus et al. 2022) diagrams is similar to that of star-forming galaxies observed at similar redshift. This means that the identification of these systems must be aided by properly designed colour-selection techniques (Natarajan et al. 2017; Valiante et al. 2018; Zhang et al. 2023; Goulding & Greene 2022; Inayoshi et al. 2022), or spectral diagnostics based on high-ionization lines, such as He II and Ne V (Nakajima & Maiolino 2022; Cleri et al. 2023), but may ultimately rely on the detection of their broad emission lines (Kocevski et al. 2023; Larson et al. 2023; Übler et al. 2023; Harikane et al. 2023a; Maiolino et al. 2023c).

In this work, we aim to assess the impact of AGN emission and Population (Pop) III/II stars on the high-redshift galaxy UV LF. We base our predictions on the Cosmic Archaeology Tool (CAT, Trinca et al. 2022), and we focus, in particular, on the redshift range probed by *JWST*, from $z \gtrsim 4$ out to ~ 16–18 (Bouwens et al. 2023; Pérez-González et al. 2023; Harikane et al. 2023b, 2024).

The paper is organized as follows. In Section 2, we summarize the mean features of CAT and the improvements made in the modelling of the first sources. In Sections 3 and 4, we present our results. In particular, we first illustrate how the model complies with global constraints on the SF (Section 3.1) and cosmic reionization histories (Section 3.3), and how our predictions compare with independent models. Then, we present the predicted redshift evolution of the galaxy LF (Section 4.1), tracing the contribution of AGNs (Section 4.2) and Pop III stars (Section 4.3) in different luminosity bins, and the potential effects of a gradual change in the stellar IMF with redshift and metallicity (Section 4.3.2). Finally, in Section 5, we summarize our findings and draw our main conclusions.

2 MODELLING THE FIRST SOURCES WITH CAT

Here, we briefly recall the main features of the CAT model, presented in detail in Trinca et al. (2022), and the improved modelling that we have made for this study (see Sections 2.2 and 2.6).

CAT is a semi-analyical model which has been developed to follow the co-evolution of the first galaxies and their nuclear BHs through cosmic times. A large sample of dark matter (DM) hierarchical merger histories, representative of the evolution of the entire galaxy population, is generated from $z = 4$ up to 24 using the GALFORM galaxy formation model (Parkinson, Cole & Helly 2008), which is based on the extended Press–Schechter formalism. To describe SF occurring in molecular and atomic-cooling haloes, corresponding to virial temperatures $1200\mathrm{K} \leq T_{\rm vir} < 10^4\,\mathrm{K}$ and $T_{\rm vir} \geq 10^4\,\mathrm{K}$, respectively, we adopt a mass resolution that corresponds to a virial temperature of $T_{\rm vir} = 1200\,\mathrm{K}$. Hence, the minimum resolved halo mass ranges from $9.4 \times 10^5\,\mathrm{M}_\odot$ at $z \sim 24$ to $1.0 \times 10^7\,\mathrm{M}_\odot$ at $z \sim 4$. Once each DM halo virializes and collapses, the gas is accreted and, depending on the virial temperature, redshift, and composition, it cools down and forms stars. The baryonic evolution is followed by means of a set of physically motivated prescriptions, that we briefly summarize below, with a set of free parameters: the star formation efficiency $\epsilon_{\rm SF}$, the BH accretion parameter α, the SN and AGN wind efficiencies $\epsilon_{\rm w,\,SN}$, $\epsilon_{\rm w,\,AGN}$ (see equations 1, 3, 7, and 8). These are calibrated to reproduce the observed stellar mass density and star

formation rate density (SFRD) at $4 \leq z \leq 6$, and the SMBHs masses and luminosities inferred for the $z \sim 6$ quasar population (for further details see section 3 in Trinca et al. 2022).

2.1 Star formation

The fraction of gas mass available for SF depends on the balance between cooling and dynamical time-scales. The SFR is computed in each galaxy as:

$$\mathrm{SFR} = f_{\rm cool}\, M_{\rm gas}\, \epsilon_{\rm SF}/\tau_{\rm dyn}, \quad (1)$$

where $M_{\rm gas}$ is the available gas mass reservoir, $\tau_{\rm dyn} = [R_{\rm vir}^3/(G\, M_{\rm halo})]^{1/2}$ is the dynamical time of the system, and $\epsilon_{\rm SF} = 0.05$ is the SF efficiency, which has been calibrated to match the SFRD and stellar mass density evolution at $4 \leq z \leq 8$ (see section 3 in Trinca et al. 2022). The parameter $f_{\rm cool}$ quantifies the reduced cooling efficiency inside molecular cooling haloes (also referred to as minihaloes) with respect to more massive atomic-cooling haloes. In fact, in minihaloes, where $T_{\rm vir} < 10^4$ K, the only efficient cooling channel in the primordial gas is provided by the roto-vibrational emission of molecular hydrogen (H_2). If the star-forming regions are exposed to a sufficiently large flux in the Lyman–Werner (LW) energy band, [11.2 − 13.6] eV, emitted by nearby galaxies, the formation of H_2 can be strongly suppressed, decreasing the cooling efficiency (Fialkov et al. 2013; Sugimura, Omukai & Inoue 2014; Valiante et al. 2016; Wolcott-Green, Haiman & Bryan 2017). Once the gas in the galaxy interstellar medium (ISM) starts to become metal-enriched due to stellar evolution, metals and dust enhance the cooling efficiency in minihaloes. Hence, the parameter $f_{\rm cool}$ in equation (1) depends on the halo virial temperature, redshift, gas metallicity, and intensity of the illuminating LW radiation. A thorough discussion of these physical dependencies of $f_{\rm cool}$ can be found in the appendix A of Valiante et al. (2016). Here, we provide a more synthetic description, and we show in Fig. 1 the value of $f_{\rm cool}$ as a function of redshift for minihaloes with $T_{\rm vir} = 2000$ and 9000 K, assuming two different values for the intensity of the illuminating LW flux ($J_{\rm LW} = 0$ and 10), and three different gas metallicities: $Z = 0$ (primordial composition), $Z = 0.1$ and $Z_\odot$ (see also fig. 1 in Sassano et al. 2021). When $J_{\rm LW} = 0$, the value of $f_{\rm cool}$ is close to unity for the most massive ($T_{\rm vir} = 9000$ K) minihaloes at high redshift, but it decreases with increasing $J_{\rm LW}$ and with decreasing metallicity. Concurrently, the cooling efficiency is reduced for smaller minihaloes ($T_{\rm vir} = 2000$ K) and it decreases toward lower redshift. Even moderate values of $J_{\rm LW}$ ($J_{\rm LW} = 10$) lead to a significant drop in the cooling efficiency, particularly for metal-free and metal-poor gas compositions. Conversely, in atomic cooling haloes we set $f_{\rm cool} = 1$.

2.2 Improved treatment of Population III stars

Relying on recent state-of-the-art hydrodynamical simulations, which follow in detail the formation of stellar systems in very metal-poor environments (Chon et al. 2021, 2022), we imposed a further requirement for the onset of SF inside pristine haloes. Since simulations suggest that cold gas clouds need to accumulate a sufficient amount of gas before undergoing collapse and fragmentation, we assumed that the cold gas mass inside each halo must be larger than a minimum value of $M_{\rm cold,min} = 10^3\,{\rm M}_\odot$ to form stars. We also adopted an enhanced SF efficiency during Pop III SF, assuming $\epsilon_{\rm SF,\,PopIII} = 0.15$, while maintaining the standard efficiency $\epsilon_{\rm SF} = 0.05$ (see Trinca et al. 2022) for subsequent stellar populations. This improved modelling sets the minimum total stellar mass formed in each Pop III SF episodes to $\sim 150\,{\rm M}_\odot$, in agreement with simulation results (Chon et al. 2022).

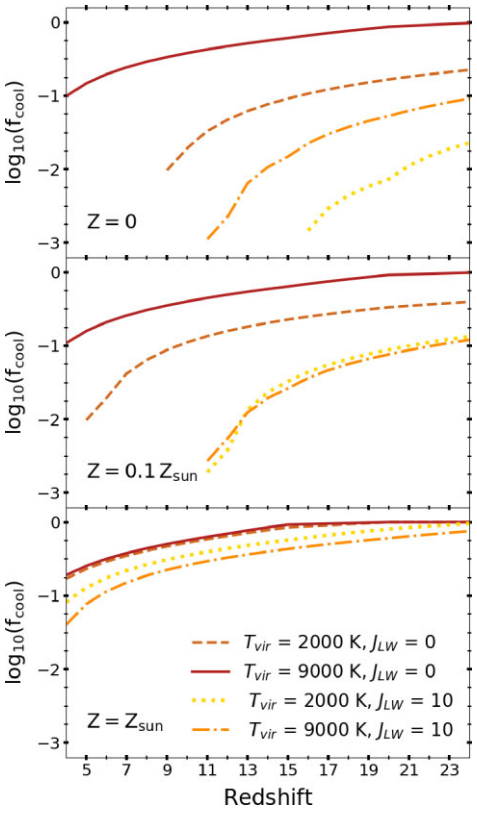

Figure 1. The mass fraction of gas that is able to cool in one free-fall time, $f_{\rm cool}$, as a function of redshift for two halo virial temperatures, $T_{\rm vir} = 2000$ and 9000 K, which enclose the minihalo mass range, and considering two different values of the illuminating LW flux, $J_{\rm LW} = 0$, 10. We show the evolution assuming three different values of gas metallicity, $Z = 0$ (upper panel), $Z = 0.1\,{\rm Z}_\odot$ (central panel), and $Z = {\rm Z}_\odot$ (lower panel).

Theoretical studies suggest that at extremely low metallicities, such as the ones characterizing the first star-forming regions, very massive stars are preferentially formed (Omukai & Nishi 1998; Bromm, Kudritzki & Loeb 2001; Omukai & Palla 2003; Yoshida, Omukai & Hernquist 2008; Hosokawa et al. 2011). The IMF of the first generation of stars, also referred to as Pop III stars, is therefore supposed to be top-heavy, with typical masses ranging from few 10s up to 100s of solar (Hirano et al. 2014; Susa, Hasegawa & Tominaga 2014; Hirano et al. 2015; Hosokawa et al. 2016; Sugimura et al. 2020). Here we assume, for Pop III stars, a Larson IMF:

$$\Phi(m_*) \propto m_*^{\alpha-1}\, e^{-m_*/m_{\rm ch}}, \quad (2)$$

where $m_{\rm ch} = 20\,{\rm M}_\odot$ is the characteristic mass, $\alpha = -1.35$ and the mass ranges between $10\,{\rm M}_\odot \leq m_* \leq 300\,{\rm M}_\odot$. Our choice is motivated by stellar archaeology studies and appears to best match the observed Galactic halo metallicity distribution function and the properties of C-enhanced and C-normal stars at [Fe/H] < -3 (de Bennassuti et al. 2014; Fraser et al. 2017; de Bennassuti et al. 2017; Magg et al. 2022; Aguado et al. 2023).

Under the environmental conditions where Pop III stars form (pristine galaxies hosted in DM minihaloes), the total stellar mass formed in a dynamical time-scale might be too small to fully sample

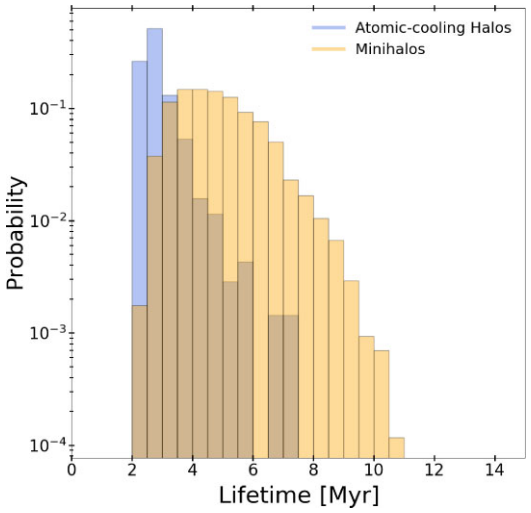

Figure 2. Distribution of lifetimes of Pop III stellar populations formed inside minihaloes (orange) and atomic-cooling haloes (blue). We show the two probability distributions assuming that the cold gas mass inside each halo must be larger than a minimum value of $M_{\rm cold,min} = 10^3\,{\rm M}_\odot$ to trigger Pop III SF. The two distributions have a different shape, reflecting the reduced amount of gas that is available for SF in minihaloes, that leads to the preferential formation of Pop III stars with masses comparable to the characteristic mass of the IMF, $m_{\rm ch} = 20\,{\rm M}_\odot$, and to an undersampling of the high-mass tail of the IMF (see the text).

the IMF of Pop III stars.[2] Therefore, we stochastically sample the IMF during each episode of Pop III SF, building up the population star by star until we saturate the total stellar mass formed. In addition, Pop III stars are often assumed to die instantaneously due to the rapid evolutionary time-scales of very massive stars. However, for less massive stars, with $m_* \sim 10\,{\rm M}_\odot$ and lifetimes $\sim 20\,{\rm Myr}$, this assumption might lead to a significant underestimation of their total radiative output, as well as of the characteristic time-scale of metal enrichment following their supernova (SN) explosions. For this reason, following each SF episode, we define the lifetime of the stellar population $\tau_{\rm life,\,PopIII}$ as the lifetime of the most massive star formed, which represents the characteristic time-scale for metal enrichment inside the host halo. As a result, multiple Pop III SF episodes can occur within the same host halo before the most massive stars explode as SN, enriching the gas above the critical threshold of metallicity $Z_{\rm crit}$, and suppressing SF due to mechanical feedback (see Section 2.4).

Fig. 2 compares the resulting distribution of stellar lifetimes for Pop III stars formed in minihaloes and atomic cooling haloes. It is evident how the distribution changes depending on the halo properties. Inside minihaloes, Pop III stars are characterized by longer lifetimes since fewer and less massive stars form. In fact, atomic cooling haloes are more massive and characterized by more efficient cooling, providing a reservoir of cold gas large enough to sample the high-mass end of the IMF ($m_* > m_{\rm ch}$), leading to shorter Pop III lifetimes. In this case, the host halo will be more rapidly enriched, promptly transitioning towards Pop II SF. At higher metallicities, emission through metal-fine structure lines and the presence of dust increase the cooling efficiency. This leads to a transition toward lower characteristic masses. Therefore, above a critical metallicity of $Z_{\rm crit} = 10^{-3.8}\,{\rm M}_\odot$, we assume that the formation of Pop II stars follows a Larson IMF, given in equation (2), with $m_{\rm ch} = 0.35\,{\rm M}_\odot$ in the mass range $[0.1, 100]\,{\rm M}_\odot$.

2.3 Black hole seeds formation and growth

At the end of each Pop III SF episode, we assume that the heaviest among the newly formed BH remnants forms a light BH seed. Inside atomic-cooling haloes (where $T_{\rm vir} \geq 10^4\,{\rm K}$), if metal and dust cooling are still inefficient ($Z \leq Z_{\rm cr}$) and molecular cooling is suppressed by a strong illuminating LW flux,[3] the gas collapses almost isothermally with no fragmentation. This leads to the formation of a single supermassive star that becomes unstable, due to nuclear exhaustion or general-relativistic (GR) instabilities, forming a heavy BH seed with a mass of $10^5\,{\rm M}_\odot$ (Hosokawa, Omukai & Yorke 2012; Latif et al. 2013; Ferrara et al. 2014; Inayoshi, Omukai & Tasker 2014; Becerra et al. 2015, 2018; Latif & Ferrara 2016). Note that we do not consider intermediate-mass BH seeds, which are supposed to from runaway mergers in dense stellar clusters (see Sassano et al. 2021, for a recent investigation that considers all the three BH seeds populations).

Once formed, BH seeds are assumed to settle at the centre of the host galaxy, where they can accrete gas and grow in mass. High-resolution zoom-in simulations show that if the BH seed mass is less than $10^5\,{\rm M}_\odot$, its dynamical evolution is very perturbed by the irregular gas and stellar distribution in high-redshift galaxies (Pfister et al. 2019; Sassano et al. 2023). This effect will further suppress the growth of light BH seeds, as discussed by Trinca et al. (2022), but have a smaller impact on the observable population of accreting BHs, which largely descend from heavy BH seeds (Trinca et al. 2023).

The gas accretion rate onto BHs is described by the Bondi–Hoyle–Lyttleton (BHL) formula (Hoyle & Lyttleton 1941; Bondi 1952):

$$\dot{M}_{\rm BHL} = \alpha \frac{4\pi G^2 M_{\rm BH}^2 \rho_{\rm gas}(r_{\rm A})}{c_{\rm s}^3}, \tag{3}$$

where $c_{\rm s}$ is the sound speed, $\rho_{\rm gas}(r_{\rm A})$ is the gas density evaluated at the radius of gravitational influence of the BH and $r_{\rm A} = 2GM_{\rm BH}/c_{\rm s}^2$. The boost factor $\alpha = 90$ is included to take into account the density enhancement at small scales around the BH and is one of the free parameters of the model, which has been calibrated to reproduce the range of BH mass and bolometric luminosity of the observed quasar population at $z > 5$ (Trinca et al. 2022).

In our reference model, the gas accretion rate, $\dot{M}_{\rm accr}$, cannot exceed the Eddington limit, so that:

$$\dot{M}_{\rm accr} = \min(\dot{M}_{\rm BHL}, \dot{M}_{\rm Edd}), \tag{4}$$

and the BH mass growth rate is computed as:

$$\dot{M}_{\rm BH} = (1 - \epsilon_{\rm r})\dot{M}_{\rm accr}, \tag{5}$$

where, $\dot{M}_{\rm Edd} = L_{\rm Edd}/(\epsilon_{\rm r} c^2)$, $\epsilon_{\rm r} = 0.1$ is the adopted radiative efficiency, and $L_{\rm Edd} = 4\pi c G M_{\rm BH} m_{\rm p}/\sigma_{\rm T}$ is the Eddington luminosity (c is the speed of light, $m_{\rm p}$ is the proton mass, and $\sigma_{\rm T}$ is the Thomson scattering cross-section).

[2] In fact, a total stellar mass of $M_{*,\rm tot} \gtrsim 10^6\,{\rm M}_\odot$ (Valiante et al. 2016) would be required to fully sample the Pop III IMF following a single SF episode.

[3] This condition is usually expressed as $J_{\rm LW} \geq J_{\rm cr}$, where $J_{\rm LW}$ is the cumulative flux into the LW energy band in units of $10^{-21}\,{\rm erg\,s^{-1}\,cm^{-2}\,Hz^{-1}\,sr^{-1}}$. For consistency with our previous studies (Trinca et al. 2022, 2023), here we adopt a threshold value of $J_{\rm cr} = 300$. A thorough discussion on the value of $J_{\rm cr}$ for heavy BH seed formation can be found in Woods et al. (2019) and Inayoshi, Visbal & Haiman (2020).

During galaxy mergers, the two nuclear BHs may sink to the centre of the newly formed galaxy, form a binary system and merge. The time-scale of this process can be considerably longer than halo sinking time-scales (Tremmel et al. 2018), but the formation of coalescing BH pairs may be facilitated if the BHs have masses $\gtrsim 10^5\,M_\odot$ and are hosted in galaxies with high central stellar and gas densities (Volonteri et al. 2020). Here, we take a very simplified approach, and assume that two BHs coalesce during major mergers, that is, if the mass ratio of their interacting host DM haloes is $\mu > 1/10$ (Tanaka & Haiman 2009; Valiante et al. 2011). Conversely, in minor mergers ($\mu < 1/10$), only the most massive among the two nuclear BHs is assumed to migrate to the centre of the newly formed galaxy. We note here that this oversimplification has a relatively small impact on BH mass growth, which is largely dominated by gas accretion (Dubois, Volonteri & Silk 2014; Valiante et al. 2016; Pacucci & Loeb 2020).

2.4 Mechanical and radiative feedback

The abundance of gas inside each galaxy is affected by mechanical feedback due to galaxy-scale outflows driven by the energy released by SN explosions and BH accretion,

$$\dot{M}_{\rm ej} = \dot{M}_{\rm ej,SN} + \dot{M}_{\rm ej,AGN}, \tag{6}$$

where $\dot{M}_{\rm ej,SN}$ and $\dot{M}_{\rm ej,AGN}$ are the SN- and AGN-driven outflow rates. The first term is defined as:

$$\dot{M}_{\rm ej,SN} = \frac{2E_{\rm SN}\epsilon_{\rm w,SN}R_{\rm SN}(t)}{v_{\rm e}^2}, \tag{7}$$

where $E_{\rm SN}$ is the explosion energy per SN, $v_{\rm e} = (2GM/R_{\rm vir})^{1/2}$ is the escape velocity of the galaxy, $\epsilon_{\rm w,\,SN} = 1.6 \times 10^{-3}$ is a free parameter representing the SN-driven wind efficiency, and $R_{\rm SN}(t)$ is the SN explosion rate. The latter quantity depends on the SF history and on the nature of the stellar populations hosted by each galaxy: for Pop III stars, $E_{\rm SN}$ is assumed to be 2.7×10^{52} erg, while for Pop II/I stars, $E_{\rm SN} = 1.2 \times 10^{51}$ erg.

The second term in equation (6) is computed as,

$$\dot{M}_{\rm ej,AGN} = 2\,\epsilon_{\rm w,AGN}\,\epsilon_r\,\dot{M}_{\rm accr}\left(\frac{c}{v_{\rm e}}\right)^2. \tag{8}$$

where $\epsilon_{\rm w,\,AGN}$ is the AGN-driven wind efficiency. Following Trinca et al. (2022), in our reference model, we assume that $\epsilon_{\rm w,\,AGN} = 2.5 \times 10^{-3}$. While quasars accreting at (or above) the Eddington limit are more likely to show strong outflows that contribute to evacuate the gas from the inner galactic regions, broad, blushifted absorption lines tracing outflowing gas have also been detected in AGNs accreting at more moderately pace, down to few per cent Eddington (see e.g. Ganguly et al. 2007). Following Trinca et al. (2022, 2023), we parametrize BH feedback as described in equation (8) even when BHs do not exceed the Eddington limit, as in the model that we discuss in this work (see also Negri & Volonteri 2017; Weinberger et al. 2017; Tremmel et al. 2019; Piana, Dayal & Choudhury 2022 for similar descriptions of BH feedback).

In addition to the radiative feedback induced by LW photons, described in Section 2.1, during the process of cosmic reionization the photoheating due to the increased gas temperature in photoionized regions can suppress SF in haloes with virial temperatures below the temperature of the intergalactic medium (IGM, Valiante et al. 2016). We consider $T_{\rm IGM} = Q_{\rm H\,II}\,T_{\rm reio} + (1 - Q_{\rm H\,II})\,T_{\rm H\,I}$, where $T_{\rm reio} = 2 \times 10^4$ K, $T_{\rm H\,I} = 0.017(1+z)^2$ and the filling factor of H II regions, $Q_{\rm H\,II}$, is computed as described below.

2.5 Metal and dust enrichment

Following Valiante et al. (2014) and de Bennassuti et al. (2014), CAT follows the metal and dust enrichment in each galaxy adopting a two-phase ISM model, with a cold atomic/molecular phase, where SF occurs and where dust grains can grow in mass by accreting gas-phase metals, and a hot/warm diffuse phase where dust can be destroyed by SN shocks. Following DM halo virialization, the gas is initially accreted into the diffuse phase, then it condenses into the cold/molecular phase, where SF occurs. Stars evolve and return gas, metal, and dust into the diffuse phase. Finally, mechanical feedback due to SN explosions and AGN eject gas from the diffuse and condensed phases, following the description provided in Section 2.4. Metal and dust enrichment in the two-phase ISM is described by a system of differential equations, which relies on mass- and metallicity-dependent metal and dust yields and follows the release of nucleosynthetic products on the stellar characteristic lifetimes. We refer the interested readers to Valiante et al. (2014) and de Bennassuti et al. (2014) for a thorough description of the chemical evolution model implemented in CAT.

2.6 Photoionizing emission and reionization

CAT follows the formation of the first stars and BHs across cosmic epochs in our galaxy sample. Therefore, we can investigate the relative contribution of different classes of sources to cosmic reionization. In particular, at different redshifts, we can compute the photoionizing emissivities from Pop II stars, Pop III stars, and early accreting BHs evolving in each galaxy of our sample.

For Pop III stars, we compute the photoionizing emission rate $\dot{n}_\gamma$ from the mass-dependent emissivities tabulated by Schaerer (2002) for zero-metallicity stars with no mass loss. For Pop II stars, we adopt the metallicity- and age-dependent intrinsic emissivities computed using Bruzual & Charlot (2003) population synthesis model. To compute the emission rate of ionizing photons from early accreting BHs, we model their spectral energy distribution (SED) as a multicolour-disc spectrum up to energies of $kT_{\rm max} \sim 1\,{\rm keV}(M_{BH}/{\rm M}_\odot)^{-1/4}$ plus a non-thermal power-law component $L_\nu \propto \nu^{-\alpha}$ with $\alpha \simeq 2$ at higher energies (Shakura & Sunyaev 1973).

Two additional effects need to be considered in order to model cosmic reionization: (i) only a fraction of the ionizing photons emitted will escape the galaxy and reach the outer medium, and (ii) the IGM density increases its inhomogeneity with time, leading to higher gas opacity to ionizing photons, and to a slower reionization process. These effects are usually modelled with two parameters that are still poorly constrained by theoretical models and observations; the escape fraction, $f_{\rm esc}$, that is, the fraction of ionizing photons that are able to escape the galaxy, and the clumping factor, C, which quantifies the increased clumpiness of the IGM.

Starting from the source emissivities, these two additional parameters allow us to predict the redshift evolution of the volume filling factor of ionized hydrogen, $Q_{\rm H\,II}$. Several works showed that a decreasing trend with redshift of $f_{\rm esc}$ is required to simultaneously accommodate the production rate of ionizing photons associated with SF and the available constraints on the IGM electron scattering optical depth τ_e. Therefore, following Dayal et al. (2020), we assume a redshift-dependent escape fraction for ionizing photons emitted by Pop II and Pop III stars:

$$f_{\rm esc,*}(z) = f_0\,[(1+z)/5]^\beta, \tag{9}$$

where we choose $f_0 = 0.03$ and $\beta = 1.5$, such that $f_{\rm esc}$ varies between ~ 3 per cent–35 per cent for $z = 4$–24. The range of values assumed

for the galaxy escape fraction is in broad agreement with empirical constraints obtained from early *JWST* observations. Recent results by Mascia et al. (2023), based on a sample of 24 lensed galaxies at $4.5 < z < 8$, suggest typical mean values of $f_{\rm esc} \sim 0.10$, while Schaerer et al. (2022) find smaller values, $f_{\rm esc} \sim 0.03$–0.08, for three systems at $z \sim 8$. For the AGN ionizing emission, instead, we make the assumption that the fraction of unobscured AGNs can be used as a tracer of the escape fraction (Ricci et al. 2017; Dayal et al. 2020). Therefore, following Ueda et al. (2014), we adopt a luminosity-dependent parametrization:

$$f_{\rm esc,AGN}(L_{\rm X}) = \min\left[f_{\rm max}, \max[f_0 - \beta(\log(L_{\rm X} - 43.75)), f_{\rm min}]\right] \quad (10)$$

with $f_{\rm max} = 0.84$, $f_{\rm min} = 0.20$, $f_0 = 0.73$, $\beta = 0.24$, and $L_{\rm X}$ is the AGN X-ray luminosity in the $[2-10]$ keV energy band (for further details, see Trinca et al. 2022).

For the IGM clumping, we rely on the parametrization proposed by Iliev, Scannapieco & Shapiro (2005), and we adopt the following redshiftdependent clumping factor:

$$C(z) = 17.6\, e^{-0.10\,z + 0.0011\,z^2}. \quad (11)$$

The time evolution of the volume filling factor for ionized hydrogen, $Q_{\rm H\,II}$, can be written as (Barkana & Loeb 2001):

$$\dot{Q}_{\rm H\,II} = f_{\rm esc}\,\dot{n}_\gamma / n_{\rm H} - \alpha_{\rm B}\, C\, n_{\rm H}\,(1+z)^3\, Q_{\rm H\,II}, \quad (12)$$

where $\dot{n}_\gamma$ is the total emission rate of ionizing photons per unit volume computed summing over all the available sources, $n_{\rm H} = X_{\rm H}\, n_{\rm IGM}$ is the number density of the hydrogen gas in the IGM, $X_{\rm H}$ is the hydrogen mass fraction, $n_{\rm IGM}$ is the IGM gas number density, and $\alpha_{\rm B} = 2.6 \times 10^{-13}\,{\rm cm^3\,s^{-1}}$ is case-B hydrogen recombination rate. From $Q_{\rm H\,II}(z)$, we can compute the IGM optical depth to electron scattering $\tau_{\rm e}(z)$ as:

$$\tau_{\rm e}(z) = \int_0^z n_{\rm e}(z')\sigma_{\rm T}\, c \left|\frac{{\rm d}t}{{\rm d}z'}\right| {\rm d}z', \quad (13)$$

where $\sigma_{\rm T} = 6.65 \times 10^{-25}\,{\rm cm^2}$ is the Thomson cross-section, c is the speed of light, and $n_{\rm e}(z')$ is the mean electron number density at z', which can be written as:

$$n_{\rm e}(z') = Q_{\rm H\,II}(z')\, n_{0,\rm B}\, X_{\rm H}(1+z)^3, \quad (14)$$

where $n_{0,\rm B} = 2.51 \times 10^{-7}\,{\rm cm^{-3}}$ is the mean baryon number density at $z = 0$.

3 GLOBAL OBSERVATIONAL CONSTRAINTS

In this section, we first describe the redshift evolution of the comoving SFRD predicted by the model. Then, we show the predicted redshift evolution of the hydrogen ionizing emissivity and neutral hydrogen fraction, and how these compare with available observational data.

3.1 Star formation history

In the upper panel of Fig. 3 we show the SFRD evolution predicted by CAT at $z > 4$. The red solid line represents the total SFRD, while the dashed and dashed–dotted red lines indicate the SFRD for galaxies with intrinsic UV magnitude $M_{\rm UV}$ smaller, that is, brighter, than -17.0 and -18.0, respectively (see also Trinca et al. 2022). We compare our results with observational constraints by Bouwens et al. (2012, 2014), Ellis et al. (2013), and Merlin et al. (2019), and with recent *JWST* data at $z \gtrsim 10$ (Bouwens et al. 2023; Donnan et al. 2023; McLeod et al. 2024; Harikane et al. 2023b). We also show the empirical relations proposed by Madau, Haardt & Dotti (2014) extrapolated to $z > 6$ (grey dashed–dotted line) and the constant SF efficiency model by Harikane et al. (2023b, maroon dotted line). In the redshift range $4 < z < 10$, CAT predictions for the total SFRD are in good agreement with data from Merlin et al. (2019), who estimated the contribution of high-redshift passive galaxies to the global SFRD during their phase of activity. It is also consistent with the SFRD estimated from ALMA large surveys, in particular from ALPINE data by Khusanova et al. (2021) and Gruppioni et al. (2020), and from REBELS data by Algera et al. (2023), and it is in very good agreement with the SFRD inferred from gamma-ray burst observations, which are sensitive to both obscured and unobscured SF (Kistler et al. 2009; Robertson & Ellis 2012). Conversely, the SFRD derived from the rest-frame UV luminosity are better reproduced by CAT when only the contribution of the sources brightest than $M_{\rm UV} \lesssim -17.0$ is considered (Trinca et al. 2022). We stress that the total SFRD computed with CAT accounts for both intrinsically faint objects and for obscured sources, which are better traced by rest-frame far-infrared observations.

3.2 Pop III star formation history

In the lower panel of Fig. 3, we also show the predicted SFRD for Pop III stars (solid orange line). The Pop III SFRD predicted by CAT is characterized by an initial steep rise at $z \gtrsim 22$, and then declines to follow a relatively flat evolution. Indeed, despite the scatter due to the intrinsic burstiness of Pop III SF, we find an almost constant SFRD of $\sim 10^{-4}\,{\rm M_\odot\,yr^{-1}\,Mpc^{-1}}$ over the redshift range $10 \lesssim z \lesssim 20$, below which the ISM metal enrichment of galaxies causes Pop III SF to become progressively rarer. In Fig. 3, we also show the Pop III SFRD predicted by high-resolution (Jaacks, Finkelstein & Bromm 2019; Liu & Bromm 2020; Skinner & Wise 2020) and large-scale (Venditti et al. 2023) hydrodynamical simulations, and the results of the semi-analytical model by Visbal, Bryan & Haiman (2020). Orders of magnitude differences are found between different studies. In particular, the mass resolution and scale of the simulations significantly affect the predicted SFRD at early times, where semi-analytical models and small-scale hydrodynamical simulations better resolve the large population of star forming minihaloes (Skinner & Wise 2020; Visbal et al. 2020). Further discrepancies can be ascribed to the different treatment of radiative feedback, which can be implemented subgrid or properly accounted for by adopting a full radiative transfer scheme (Maio et al. 2016; Xu et al. 2016). Likewise, the implementation of chemical evolution can vary among different studies, with only few models adopting mass and metallicity-dependent stellar yields and accounting for the presence of cosmic dust. Finally, distinct assumptions are made in different simulations regarding the Pop III stellar IMF and the critical metallicity threshold for Pop II SF (see e.g. Venditti et al. 2023, for a detailed discussion). CAT results appear to be in broad agreement with high-resolution simulations (Jaacks et al. 2019; Skinner & Wise 2020), which tend to predict larger SFRDs, especially in the redshift range $10 < z < 20$. This might be related to the ability of resolving Pop III SF in small DM minihaloes, which are generally below the resolution threshold of large-scale simulations (Sarmento & Scannapieco 2022; Venditti et al. 2023). Interestingly, the Pop III SFRD predicted by CAT is in very good agreement with the predictions of Skinner & Wise (2020) down to $z \sim 12$, below which their SFRD quickly decreases, due to the strong impact of LW radiation inside the simulated $1\,{\rm Mpc^3}$ comoving box. The high Pop III SFRD predicted by CAT at $z > 22$ is a consequence of the lack of self-regulation in the early star-forming regions hosted by the first minihaloes. The description of Pop III SF in these systems implemented in CAT accounts for the stochasticity in their IMF, and the population is evolved over the

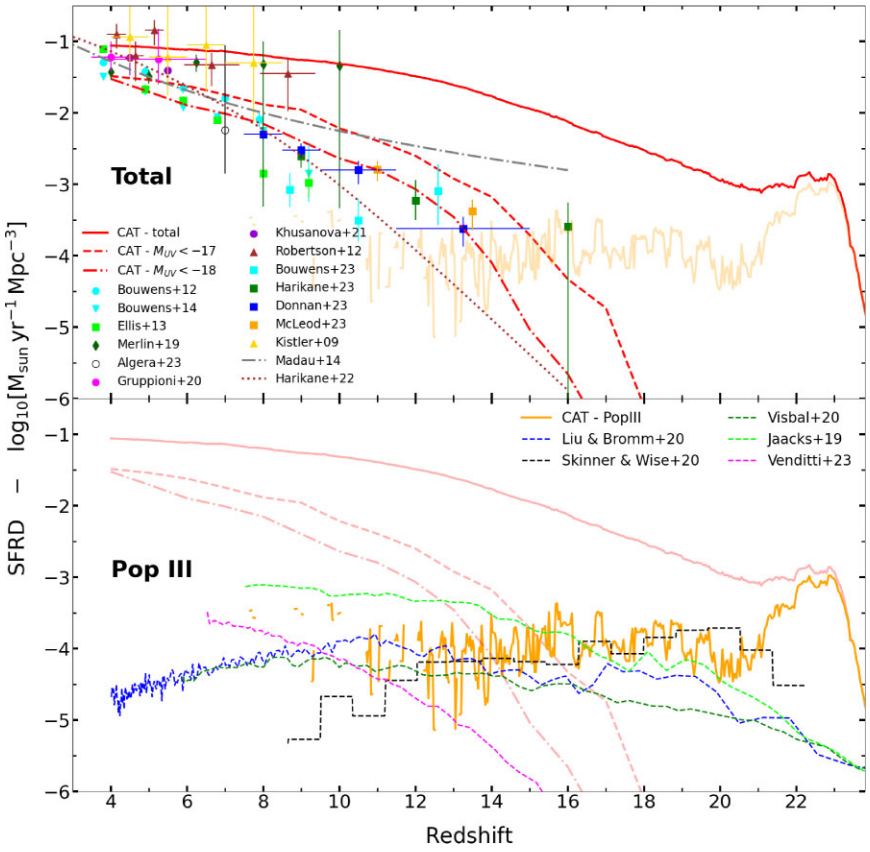

Figure 3. Evolution of the global (PopIII + PopII, upper panel) and PopIII-only (lower panel) SFRD as a function of redshift. In the upper panel, CAT predictions illustrate the total SFRD (solid red lines) and the SFRD of UV-bright sources with $M_{UV} < -17$ (red dashed line) and $M_{UV} < -18$ (red dashed–dotted line). The SFRD inferred from observations sampling the rest-frame UV luminosity are taken from Bouwens et al. (2012, 2014), Ellis et al. (2013), and Schenker et al. (2013) and from recent *JWST* data (Bouwens et al. 2023; Donnan et al. 2023; McLeod et al. 2024; Harikane et al. 2023b). In addition, we also show the SFRD derived by (Merlin et al. 2019) from the SFRHs of passive galaxies during their active phase, by ALMA large surveys (Gruppioni et al. 2020; Khusanova et al. 2021; Algera et al. 2023), and by gamma-ray bursts observations (Kistler et al. 2009; Robertson & Ellis 2012), which are sensitive to both obscured and unobscured SF. Finally, we also show the extrapolation of the empirical models by Madau et al. (2014) and the constant SF efficiency model by Harikane et al. (2023b). In the lower panel, we compare the Pop III SFRD predicted by CAT with independent theoretical models by Jaacks et al. (2019), Liu & Bromm (2020), Skinner & Wise (2020), Visbal et al. (2020), and Venditti et al. (2023). For illustrative purposes, we also report CAT predictions for the global and PopIII-only SFR density with fainter colours in the lower and upper panels, respectively.

typical lifetimes of the more massive stars formed; these masses are generally smaller in minihaloes than in Lyman-alpha cooling haloes (see Fig. 2), as a result of the reduced gas mass available for SF. Because of this, mechanical feedback acts on longer timescales. Once feedback becomes efficient, SF begins to self-regulate, as indicated by the descending trend of the SFRD at $z \lesssim 22$, only $\sim$20 Myr after the first star-forming episodes at $z = 24$. Different assumptions are made in other semi-analytical models. For instance, in the work by Visbal et al. (2020), a constant time delay of 10 Myr is assumed after the first episode of Pop III SF before subsequent metal-enriched SF can occur, to account for the gas recovery time after SN explosions. This different treatment of Pop III SF can account for the large discrepancy in the predicted SFRD at very early times, before stellar feedback starts to efficiently self-regulate the SF process, leading to much closer trends at $z \lesssim 20$.

3.3 Cosmic reionization

In Fig. 4, we illustrate the reionization history predicted by CAT, with the relative role played by different sources of ionizing photons. In the upper panel, we show the evolution in redshift of the global photoionizing emissivity, that is, the rate of ionizing photons injected into the IGM by the entire galaxy population. Different coloured lines represent the contribution of Pop II stars (solid brown), Pop III stars (solid yellow), and AGNs (blue dashed), which we assume to include the entire population of early accreting nuclear BHs. For all sources, the intrinsic photon rates are corrected for the adopted escape fractions (equation 9 for Pop II and Pop III stars and equation 10 for AGNs).

The emissivity of Pop III stars initially rises quickly and peaks at $z \sim 20$, to remain then almost constant with $\dot{n}_{\gamma,\mathrm{PopIII}} \sim 10^{49}$–$10^{50}\,\mathrm{s^{-1}\,Mpc^{-1}}$, closely tracing the Pop III SFRD evolution, down to the last few episodes of Pop III SF at $z \sim 10$. The contribution of Pop II stars shows a smooth increase from $z \sim 23$ to ~ 12, below which it slowly declines, despite the increasing trend of the Pop II SFRD, as a consequence of the decrease in the escape fraction $f_{\mathrm{esc}}(z)$. The parametric evolution of $f_{\mathrm{esc}}(z)$ described by equation (9), translates into values of $f_{\mathrm{esc}} \simeq 0.04$, 0.10, and 0.25 at $z = 5$, 10, and 20, respectively. Despite the large uncertainties that still affect observational constraints, these values are consistent with recent results (Schaerer 2002; Finkelstein et al. 2019; Naidu et al. 2020; Mascia et al. 2023), which suggest a global averaged escape fraction between 5 per cent − 10 per cent at $z < 10$, and a rising emissivity

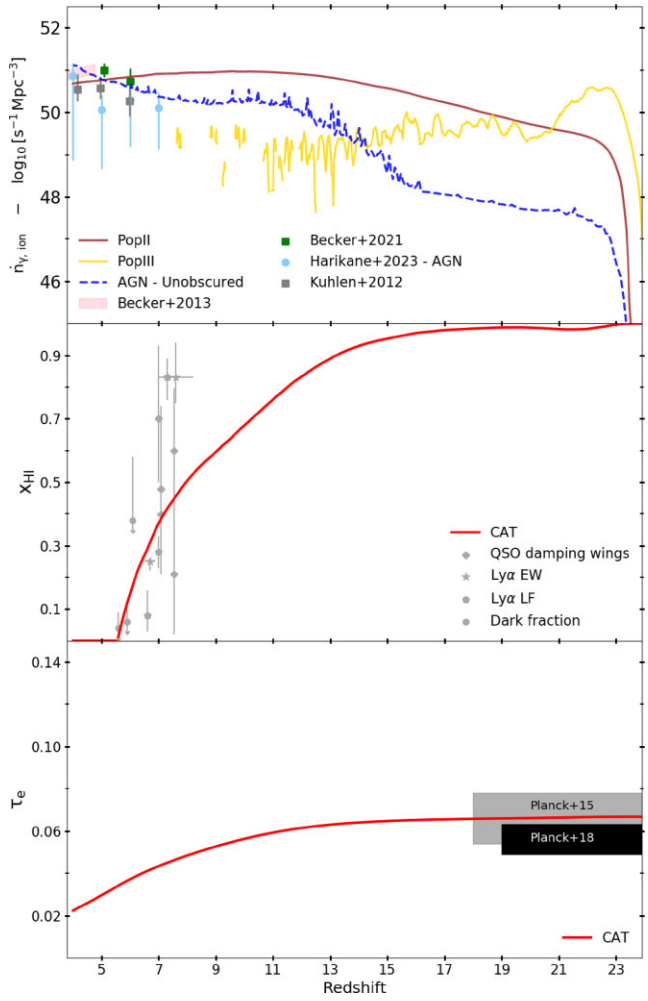

Figure 4. Upper panel: global photoionizing emissivity as a function of redshift. Brown solid, yellow solid, and blue dashed lines represent the contribution of PopII stars, PopIII stars and unobscured AGN, respectively, to the global emissivity. We show as a reference the empirical constraints proposed by Kuhlen & Faucher-Giguère (2012, grey data points), Becker & Bolton (2013, pink-shaded region), Becker et al. (2021, green data points), and the recent estimates of the AGN contribution obtained by Harikane et al. (2023a, light blue circles). Central panel: evolution of the IGM neutral hydrogen fraction as a function of redshift. CAT predictions are compared to a compilation of observational constraints presented in Bolan et al. (2022), and obtained through different tracers, such as the evolution of Lyman-α equivalent width (Bolan et al. 2022, stars), Lyman-α LF (Morales et al. 2021, pentagons), the dark pixel fraction in the Ly-α and Ly-β forest (McGreer et al. 2015, circles), and quasar damping wings (Davies et al. 2018; Greig et al. 2019; Wang et al. 2020, diamonds). Bottom panel: predicted evolution of the Thomson scattering optical depth as a function of redshift, compared with constraints obtained by the *Planck* cosmological survey (Planck Collaboration XIII 2016; Planck Collaboration VI 2020).

with increasing redshift throughout the epoch of reionization. It is interesting to note that the Pop II emissivity starts to significantly dominate over the Pop III contribution only at $z \lesssim 16$, when the SFRD of Pop III stars is already ~ 2 dex below the Pop II one (see Fig. 3). This is a result of the different stellar IMF and metallicity of the two populations, with massive and very massive Pop III stars having much harder spectra and higher ionizing photon emissivities per unit stellar mass.

In our reference model, stars are the primary source of ionizing photons in the IGM. At $z \gtrsim 15$, the BHs hosted in galaxy nuclei are descendants of light seeds, with typical initial masses of $M_{\rm BH} \lesssim 10^3$ M$_\odot$. Their mass growth proceeds in the Bondi–Hoyle gas accretion regime, and is highly inefficient, as shown in Trinca et al. (2022). As a consequence, the first accreting BHs at $z > 15$ are intrinsically faint sources of photoionizing radiation. At $z \lesssim 15$, heavy BH seeds form, with masses $M_{\rm BH} = 10^5$ M$_\odot$, and their gas accretion is more efficient. As a result, the AGN ionizing emissivity starts to increase, but remains subdominant with respect to the Pop II stellar emission down to $z \sim 5$.

In the redshift range $4 < z < 6.1$, the photoionizing emissivity predicted by CAT is in good agreement with the empirical constraints on the ionizing UV background obtained by Becker & Bolton (2013) and Becker et al. (2021), with unobscured AGNs (blue dashed line) providing the dominant contribution only at $z < 5$. The predicted AGN emissivity appears to be consistent with the recent estimates from Harikane et al. (2023a), based on the first census of 10 faint broad-line AGNs at $z \sim 4$–7 detected in early *JWST* observations.

In the central panel of Fig. 4, we show the IGM fraction of neutral hydrogen, $x_{\rm H\,I} = 1 - Q_{\rm H\,II}$, predicted by CAT (red solid curve), compared with empirical constraints presented by Bolan et al. (2022, grey data points) and obtained with different inference methods, based on Lyman-break galaxy (LBG) samples (Morales et al. 2021; Bolan et al. 2022), constraints from the dark pixel fraction in the Ly-α and Ly-β forest (McGreer, Mesinger & D'Odorico 2015), and quasar damping wings (Davies et al. 2018; Greig, Mesinger & Bañados 2019; Wang et al. 2020). We find that the ionization process is complete around $z \sim 5.5$, in agreement with the end of the reionization epoch expected from observational constraints. In addition, we find a good agreement with observations at $z \lesssim 8$, although it is important to notice that empirical estimates at $z > 7$ are inferred from different tracers and show a large scatter. In particular, analysis based on damping wings of bright quasars (Davies et al. 2018) suggest a lower neutral fraction at $z \sim 7.5$ with respect to estimates obtained from LBG samples, and are in closer agreement with CAT predictions. These uncertainties in the higher redshift range will improve with forthcoming deep *JWST* surveys at $z = 7$–10, which will put tighter constraints on the evolution of the IGM neutral fraction with combined photometric and spectroscopic data.

Finally, the lower panel of Fig. 4 shows the evolution of the electron scattering optical depth $\tau_{\rm e}$, compared to recent constrains obtained by the *Planck* cosmological survey and, in particular, with the results from Planck Collaboration VI (2020). We find a value $\tau_{\rm e,CAT} = 0.067$, which is consistent within 2σ with the *Planck* estimates $\tau_{\rm e,Planck} = 0.054 \pm 0.007$.

4 PREDICTING GALAXY UV EMISSION

In the previous sections, we showed that CAT model predictions appear to be consistent with current constraints on the redshift evolution of the SFRD and the history of cosmic reionization. The natural extension of this analysis is therefore to characterize the luminosity distribution of the population of high-redshift galaxies, and follow its evolution in time. In what follows, we present CAT model predictions for the galaxy UV LF at $4 \leq z \leq 16$, considering the contribution of stellar populations – including Pop III stars-, BH accretion, and the effects of a gradual change in the stellar IMF with redshift and metallicity, as suggested by recent hydrodynamical simulations (Chon et al. 2021, 2022).

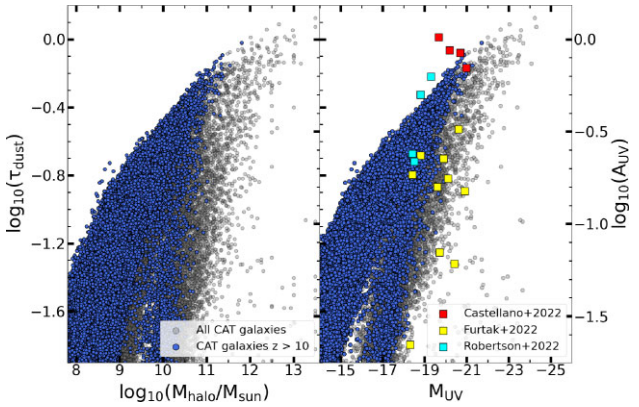

Figure 5. Predicted values of $\tau_{\rm dust}$ (left axis) and $A_{\rm UV}$ (right axis) as a function of the halo mass (left panel) and UV magnitude (right panel). The properties of the galaxy population predicted by CAT at $z > 10$ (blue circles) are compared with the results obtained for high-z galaxies observed with *JWST* by Castellano et al. (2023), Furtak et al. (2023), and Robertson et al. (2023). As a reference, we also show with grey data points the values predicted by CAT for the galaxy population at all redshifts.

4.1 Galaxy UV luminosity function at $4 \leq z \leq 16$

For this study, we improve our modelling of the total UV emission arising from each galaxy with respect to what has been presented in Trinca et al. (2022), where the galaxy intrinsic UV luminosity was obtained from the SFR adopting a standard conversion factor (Madau & Dickinson 2014).

We compute the UV luminosity of each galaxy, $L_{\rm UV,*}$, by summing over the emission of its active stellar populations, adopting age and metallicity-dependent SEDs, as explained in Section 2.6. Following Mancini et al. (2016), we account for dust obscuration by correcting the galaxy UV luminosity as:

$$L_{\rm UV,obs} = L_{\rm UV}\ \exp[-\Sigma_{\rm gas}\,\mathcal{D}\,k_{\rm UV}], \tag{15}$$

where $\Sigma_{\rm gas} = M_{\rm gas}/\pi r_{\rm d}^2$ is the gas surface density within a radius $r_{\rm d} = 0.18\,r_{\rm vir}$ (Mo, Mao & White 1998), $\mathcal{D}$ the dust-to-gas mass ratio, and $k_{\rm UV}$ is the extinction coefficient per unit mass in the energy band of interest. The value of $k_{\rm UV}$ has been inferred considering the extinction curve of the Small Magellanic Cloud (Weingartner & Draine 2001). Since CAT is able to track the fraction of the ISM that resides in the warm/hot diffuse medium (see Section 2.5), we assume here a simple screen model, where the optical depth is computed considering the contribution of the diffuse gas and dust mass inside the galaxy. However, this modelling may appear oversimplified if compared to more sophisticated two-phase dust extinction models (see e.g. Mancini et al. 2016), and may underestimate the impact of dust obscuration. Indeed, the increased compactness of high-redshift galaxies would result in lower values of $r_{\rm d}$, leading to a larger column density and dust optical depth. At the same time, while here we assume every galaxy to form a disc, these early systems are expected to show more complex morphologies and dust distributions, with UV dark and bright regions within the same system. For these reasons, the dust obscuration provided by our model has to be considered as an average over systems with comparable halo masses, but very likely different relative stellar/dust geometries and dust optical depths. In Fig. 5, we show the attenuation predicted by CAT (grey points) as a function of the host halo mass (left panel) and UV magnitude (right panel), highlighting the systems at redshift $z > 10$ (blue points). When compared with the extinction values derived by Castellano et al. (2023), Furtak et al. (2023), and Robertson et al. (2023) for a sample of high-redshift galaxies observed with *JWST* at $z \gtrsim 9$, we see that – despite representing a lower limit to the potential dust obscuration – our simplified approach predicts a range of values consistent with the observations.

In Fig. 6, we show the predicted evolution of the galaxy UV LF in the redshift range $4 \leq z \leq 16$. Here, we only consider the UV luminosity coming from stellar emission, $L_{\rm UV,*}$ (i.e. we do not consider the additional contribution to the UV emission from accreting BHs). At $z > 10$, given the restricted number of sources currently observed and the potential uncertainties in their redshift determination, we decided to show the galactic LF predicted by CAT averaged over three redshift ranges $10 < z < 11$, $12 < z < 13$, and $14 < z < 16$.

CAT results are compared to several observational data (see Harikane et al. 2023b, and references therein), including results coming from *JWST* observations (Finkelstein et al. 2022; Castellano et al. 2023; Donnan et al. 2023; Pérez-González et al. 2023; Robertson et al. 2023; Adams et al. 2023a; Harikane et al. 2023b, 2024). The model predictions are in good agreement with observational data in the redshift range $z \simeq 4$–9.

At $z \sim 10$–13, the mild evolution observed in the galaxy LF is well reproduced by CAT, except for the bins of highest luminosity, at $M_{\rm UV} < -19$, where, despite the large statistical uncertainties, the galaxy number density predicted by the model is smaller than the value inferred by some observational studies. These, however, show significant variations, depending on the surveyed area and *JWST* program considered, hinting to the potential presence of galaxy overdensities in some of these fields (Castellano et al. 2023), to the effect of cosmic variance (Yung et al. 2024; Adams et al. 2023b), as well as to the possible contamination of low-redshift systems in the photometric samples (Naidu et al. 2022; Arrabal Haro et al. 2023; Zavala et al. 2023).

Finally, at $z \sim 14$–16, CAT predictions are compared with the recent constraints from Harikane et al. (2023b) and Bouwens et al. (2023), based on two candidate galaxies with estimated redshift $z_1 = 16.25^{+0.24}_{-0.46}$ and $z_2 = 16.41^{+0.66}_{-0.55}$. At this very early epoch, the model predicts a number density of bright galaxies that appears to be significantly lower with respect to what is suggested by *JWST* observations, with a number density of sources with $M_{\rm UV} \sim -20$, which is ~ 1.2 dex lower than the best-fitting distribution obtained by Harikane et al. (2024) assuming a Schechter function (see also Fig. 12 for a quantitative comparison). It has to be noted, though, that if the spectroscopic confirmation were to favour redshift values on the lower bound of the uncertainty range, CAT predictions would stand at $\sim 1\sigma$ from the constraint proposed by Harikane et al. (2024). In addition, we also show the best-fitting distribution obtained by Harikane et al. (2023b) at $z \sim 16$, where they perform the analysis considering only sources with a spectroscopic confirmation. Given the lack of any spectroscopically confirmed galaxy at $z > 14$, they extrapolated the best-fitting Schechter function obtained for $z \sim 9$–12 toward higher redshift. In this case CAT predictions for $M_{\rm UV} \leq -19$ are consistent with the observed LF, which, however, needs to be interpreted as a lower limit. Hence, spectroscopic identification of galaxy candidates observed at $z \simeq 14$–16 will be crucial to confirm the excess of UV bright sources compared to current model predictions. CAT predictions are also compared with recent observational constraints on the galaxy LF at $M_{\rm UV} \sim -18$ by Robertson et al. (2023), based on the photometric detection of three candidate galaxies at $z > 13.5$. Interestingly, the number density predicted by CAT is in good agreement with the data at these fainter luminosities.

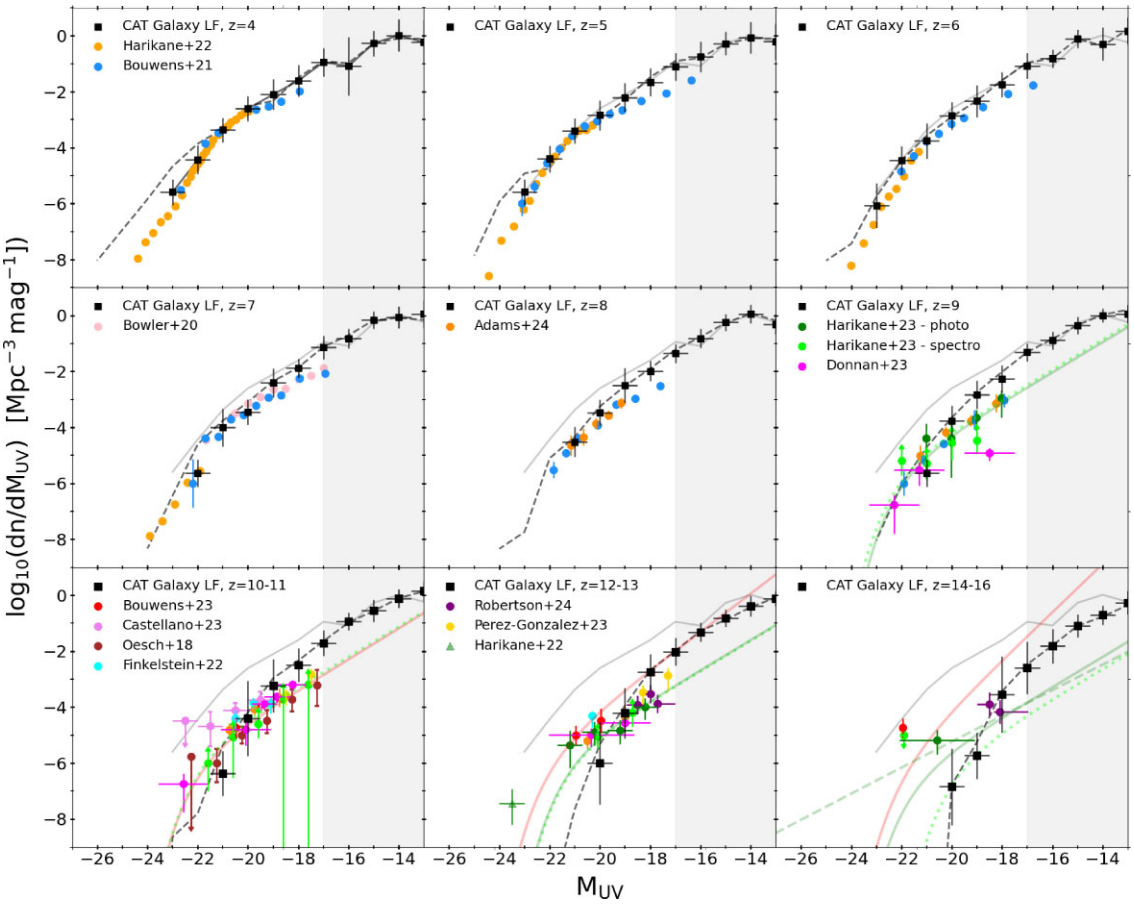

Figure 6. Observable (obscuration-corrected) galaxy UV LF between $z = 4$ and 16. CAT predictions for the dust-corrected (black data points) and intrinsic (black dashed lines) distributions are compared with observational data from Oesch et al. (2018, brown), Bowler et al. (2020, pink), Bouwens et al. (2021, blue), Bouwens et al. (2023, red), Harikane et al. (2022a, 2023b, dark green), Harikane et al. (2024, light green), Finkelstein et al. (2022, 2023, cyan), Harikane et al. (2022b, orange), Donnan et al. (2023, magenta), Adams et al. (2023a, dark orange), Castellano et al. (2023, violet), Robertson et al. (2023, dark violet), and Pérez-González et al. (2023, yellow). The figure shows that stellar emission can account for the observed UV luminosity evolution from $z \sim 4$ to ~ 10. At higher redshifts, similar to other standard galaxy formation models, CAT predictions fail to account for the UV bright end of the LF sampled by *JWST* observations. The grey-shaded area highlights the population of sources with $M_{\rm UV} > -17$, which contribute to the unresolved SFRD shown in Fig. 3. In all panels, we show as a reference the UV LF predicted by CAT at $z = 4$ (solid grey lines) for an easier comparison with the distribution at higher redshift. In the lower panels, we also show the best-fitting distributions obtained by Bouwens et al. (2023, $z \sim 10$, 13, and 17, red lines) and Harikane et al. (2023b, $z \sim 9$, 12, and 16, green lines), assuming a Schechter function (solid) or a double power-law (dashed) distribution. The light green dotted lines report instead the best fit of the LF at $z \sim 9$, 10, 12, and 16 obtained by Harikane et al. (2024) considering only galaxies with a spectroscopic confirmation.

To evaluate the potential impact of dust obscuration in the comparison between CAT predictions and observational constraints, we overplot in Fig. 6 the intrinsic galaxy UV LF at different redshifts as black dashed lines. It is clear how dust attenuation mostly affects the range of luminosity covered by the galaxy population, while it does not affect the overall normalization of the distribution. Indeed, only the bright end of the LF in the lower redshift range, $z \lesssim 7$, is significantly lowered when accounting for obscuration, and at $z \gtrsim 10$ even the intrinsic distribution cannot reproduce the high number density of bright galaxies observed by *JWST*. In the following section, we will explore whether the contribution to the UV luminosity from accreting BHs can partially relieve the current tension between CAT predictions and the bright end of the UV LF at $z \sim 14$–16 derived from photometric candidates (Bouwens et al. 2023; Harikane et al. 2024).

4.1.1 Evolution of the galaxy faint end

An interesting prediction of the CAT model is the number density of sources fainter than $M_{\rm UV} = -17$ at redshift $z \gtrsim 9$, which appears to be larger than the value obtained by extrapolating the faint end of the observationally estimated LF. This might be due to the incompleteness of the observed samples at these faint magnitudes, or to a higher impact of dust attenuation (see e.g. Barrufet et al. 2023). At the same time, it may point to a too efficient rate of SF or to a too inefficient feedback in the galaxies populating the faint end of the galaxy UV LF at these epochs in our model. We also note that, at these faint magnitudes, the UV LF predicted by CAT shows a very mild evolution between $z \sim 14$–16 and $z = 4$, which can be appreciated in Fig. 6 by comparing the predicted LF at $z > 4$ with the light grey solid line, which represents the LF predicted at $z = 4$. This is an interesting prediction of the model, reflecting the interplay of different physical processes during the evolution of fainter star forming systems. To investigate more closely this low luminosity regime, in Fig. 7 we show the predicted evolution in redshift of the cumulative number density of galaxies with $-17 < M_{\rm UV} < -10$. At early times, a progressive increase in the number density of faint galaxies is observed down to $z \simeq 12$. This reflects the widespread availability of gas in the early phases of galaxy evolution, and the

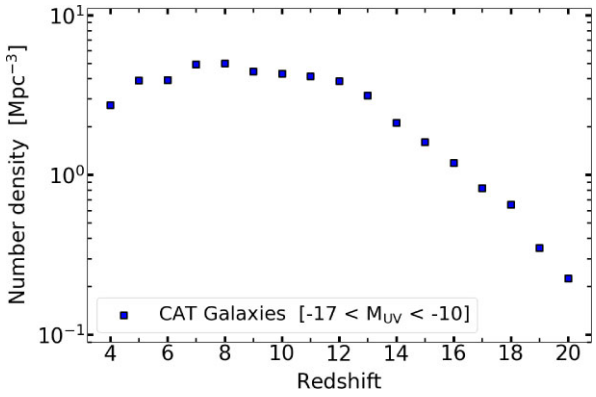

Figure 7. Redshift evolution of the cumulative number density of galaxies with $-17 < M_{UV} < -10$ predicted by CAT.

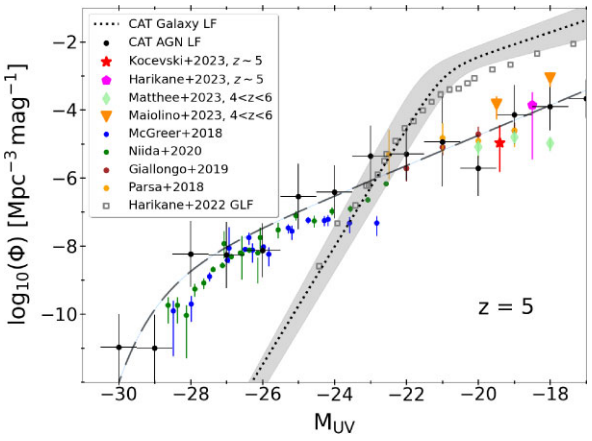

Figure 8. UV LF predicted by CAT for the AGN and galaxy population at redshift $z = 5$. Similarly to Fig. 6, the galaxy LF is computed considering only the emission from stellar populations (the dotted line and grey-shaded region represent, respectively, the best fit and 1σ spread of the distribution), and it is compared with observations from Harikane et al. (2022a, empty grey squares). The AGN LF is shown by the black filled dots, and fitted with the black dashed line. This is compared to observations by McGreer et al. (2018), Parsa et al. (2018), Giallongo et al. (2019), Niida et al. (2020), and to the recent estimates based on *JWST* data by Kocevski et al. (2023), Harikane et al. (2023a), Matthee et al. (2023), and Maiolino et al. (2023c). CAT model predictions are in good agreement with available constraints at $z = 5$.

increasing fraction of faint galaxies hosting active Pop III stellar populations (as it will be further discussed in Section 4.3), which can boost the UV luminosity of less massive galaxies. At later times, the number density of faint galaxies remains almost constant, tracing a plateau which extends between $8 \lesssim z < 12$. This behaviour reflects the increasing importance of mechanical feedback due to SNe in regulating SF of less massive systems. In addition, the gradual build up of the Lyman–Werner background leads to a decrease in the SF efficiency of minihaloes and, consequently, of the galaxy number density at the faint end. At $z \lesssim 8$, the number density starts to mildly decline, leading to a reduction in the number density of faint galaxies of 50 per cent between $z = 8$ and 4. This effect is due to photoheating of reionized regions, which prevents gas accretion onto minihaloes. The net result of this evolution is a faint-end slope of the UV LF which increases by $\lesssim 1$ dex from $z \sim 16$ to $z = 4$. A similar mild evolution has been recently obtained also by Williams et al. (2023). Performing detailed hydrodynamical simulations, they found that streaming velocities, that is, the supersonic relative motions between DM and baryonic overdensities, have a strong impact in enhancing the faint end of the LF at $z \sim 12$, since the suppression of SF inside small haloes at very early times leads to brighter dwarf galaxies at later times. While this is an intriguing result on its own that needs additional analysis, in the following sections we primarily focus on the model predictions for the bright end of the galaxy LF, at $M_{UV} < -18$.

4.2 Can BH accretion explain the UV luminosity function at $z > 10$?

In addition to stellar emission, we also account for the possible contribution of the UV luminosity emitted by the nuclear BH, $L_{UV,\,AGN}$. In fact, for high-redshift systems, AGN contamination in the UV rest-frame emission might be significant (Pacucci et al. 2022), as we will analyse more in detail below. From the BH accretion rate (see equation 3), we estimate the BH bolometric luminosity as:

$$L_{bol} = \epsilon_r \dot{M}_{accr} c^2, \tag{16}$$

and then convert this into the UV luminosity relying on the bolometric correction proposed by Duras et al. (2020), and assuming $L_\nu \propto \nu^{-0.44}$ (as described in detail in Trinca et al. 2022).

A thorough comparison between the AGN LF predicted by CAT in the UV and X-ray bands has been presented by Trinca et al. (2022), finding a good agreement between our reference model prediction and the available observational constraints. To provide an example, here we show in Fig. 8 the predicted AGN UV LF at $z = 5$ (filled black data points and black dashed line). This is compared to observational constraints from McGreer et al. (2018) and Niida et al. (2020) at the bright end ($M_{1500} < -22$), and from Parsa, Dunlop & McLure (2018), Giallongo et al. (2019), Kocevski et al. (2023), Harikane et al. (2023a), Maiolino et al. (2023c), and Matthee et al. (2023) at the faint-end. We also show the galaxy UV LF predicted by CAT (the black dotted line and grey-shaded region represent, respectively, the double power-law best fit and 1σ spread of the distribution) and observed (empty grey squares, Harikane et al. 2022a). The comparison confirms that CAT model predictions are in good agreement with the observed galaxy and AGN UV LF at $z = 5$, reproducing remarkably the surprisingly high number density of faint AGNs suggested by the most recent estimates based on *JWST* data (Greene et al. 2023; Matthee et al. 2023; Maiolino et al. 2023c).

We then recompute the UV LF considering both emission from stars and accreting BHs, $L_{UV,*} + L_{UV,\,AGN}$ at $z = 4$–16, and estimate the mean and maximum contribution of the AGNs to the total galaxy emission in different ranges of magnitude. This is shown in Fig. 9.

At $z = 4$–9, the total (galaxy + AGN) UV LF predicted by CAT is compared to the fit of the combined LF for both AGN and star-forming galaxies derived by Finkelstein & Bagley (2022), finding a good agreement. At $z \geq 10$, we compare our predictions with the best-fitting distributions proposed by Bouwens et al. (2023) and Harikane et al. (2024), also shown in Fig. 6. On average, we find that the contribution of accreting BHs to the galaxy UV luminosity is negligible at these redshifts (see the filled histograms). At $10 \lesssim z \lesssim 15$, during the formation epoch of heavy BH seeds, the AGN emission contributes on average to ~ 1 per cent–3 per cent of the total UV emission, with the largest contribution being at most $\lesssim 10$ per cent in the brightest bins of magnitude, at $M_{UV} \lesssim -19$ (see the empty histograms). At even higher redshifts, $z \gtrsim 15$, the AGN emission is even smaller, due to the stunted growth of light seeds predicted by our reference model (see Trinca et al. 2022). Considering the joint UV emission of stars and accreting BHs, we still find that the number density of systems with $M_{UV} \sim -20$ predicted by CAT is ~ 1.2 dex

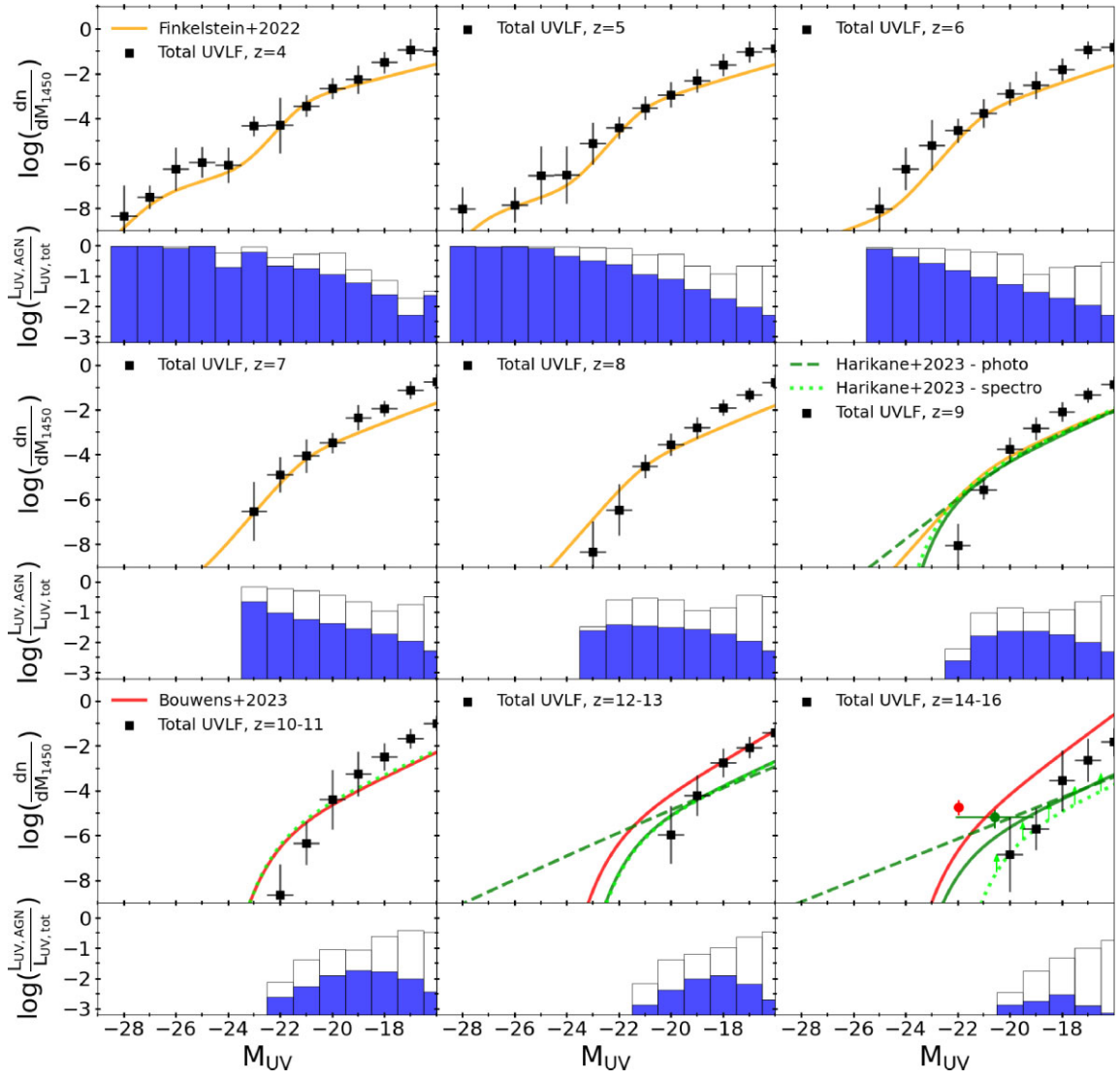

Figure 9. Observable (obscuration-corrected) global UV LF (galaxy + AGN) predicted by CAT at $z = 4$, 5, 6, 7, 8, and 9 and in the redshift ranges $10 \leq z \leq 11$, $12 \leq z \leq 13$, and $14 \leq z \leq 16$ (from top left to bottom right). For each panel, we also show the mean (filled histograms) and maximum (empty histograms) AGN contribution to the total UV luminosity (galaxy + AGN) in each magnitude bin. In the upper panels, CAT predictions are compared with the compilation of observational data presented by Finkelstein & Bagley (2022) for the global UV LF. In the lower panels, we show instead the best-fitting distributions obtained by Bouwens et al. (2023) ($z \sim 10$, 13, and 17, red lines) and Harikane et al. (2023b, 2024) ($z \sim 9$, 10, 12, and 16, green lines) based on observational constraints on the UV LF at $z \gtrsim 9$ coming from recent *JWST* data.

lower than the best-fitting distribution obtained by Harikane et al. (2024) assuming a Schechter function, similarly to what was found when only stellar emission was considered. At the same time, model predictions closely match the distribution obtained by Harikane et al. (2023b) considering only spectroscopically confirmed galaxies (see Fig. 12).

At $7 \lesssim z \lesssim 10$, we observe a growing impact of AGNs to the total UV emission, with an average contribution between 1 per cent − 20 per cent of the galaxy luminosity, and peaks of maximum contribution reaching > 50 per cent of the total emission, especially in the brightest luminosity bins. Finally, at $z < 7$, we predict the AGN population to dominate the bright end of the total UV LF, accounting on average for 20 per cent − 100 per cent of the emission coming from systems brighter than $M_{\rm UV} - 22$. The average AGN contribution decreases for fainter galaxies, where it appears to be subdominant, though it might still reach > 50 per cent of the total UV emission for specific systems.

We thus find that the AGN contribution does not have a significant impact on the emission of $z \gtrsim 10$ galaxies, and it cannot resolve the discrepancy between model predictions and observations on the number density of bright sources with $M_{\rm UV} < -19$. However, while the AGN UV luminosity appears to be – on average – subdominant in fainter high-redshift galaxies, detailed selection criteria applied to deep *JWST* surveys (Trinca et al. 2023) might be able to identify systems hosting the brightest and more luminous BHs from the general population (Goulding & Greene 2022; Nakajima & Maiolino 2022; Volonteri et al. 2023), enabling to constrain their contribution to the total LF.

Recent works advocated for super-Eddington accretion to explain the observed deviation from the local scaling relation $M_{\rm BH}/M_*$ of the population of high-redshift AGNs. This could be relevant to interpret

the bright excess observed in the galaxy UV LF, since the presence of BHs accreting very efficiently already at early epochs might in principle provide a higher contribution to the global emission of the host galaxy with respect to what is shown in Fig. 9. In a recent work (Schneider et al. 2023), we compared our model predictions for the population of accreting BHs with recent *JWST* observations of $z > 5$ AGNs for both an Eddington-limited and a super-Eddington BH growth scenario, where brief periods of enhanced accretion are assumed to be triggered during major galaxy mergers. Both models are able to account for current observations of extreme BH candidates at $z > 8$, despite a super-Eddington accretion history predicts a significantly higher number density of massive systems at these high redshifts, and they both provide similar predictions for the bright end of the AGN LF (see Trinca et al. 2022). However, given the typical short time-scales of the super-Eddington accretion phase, on the order of a few Myr, even in this alternative growth scenario it is unlikely that accreting BHs will provide a significant boost to the galaxy LF at early times. A more thorough study is however required to support this conclusion and hence we defer a deeper analysis to a future work, where we will implement a more refined treatment of the super-Eddington accretion mechanism to investigate its potential impact on the overall galaxy evolution through cosmic time.

4.3 Can a top-heavy IMF explain the UV luminosity function at $z > 10$?

The UV emissivity of stellar populations is very sensitive to their IMF, metallicity, and ages. Mason et al. (2023) argue that current $z \gtrsim 10$ galaxies observed by *JWST* are dominated by systems with young ages ($\lesssim 10$ Myr) and high SFRs. Harikane et al. (2024) show that, for a given SFR, the UV luminosity from Pop III stars characterized by a top-heavy IMF is ∼3–4 times larger than that of Pop II stars with a normal Salpeter-like IMF. Here, we first discuss CAT model predictions regarding the UV emission from Pop III stars, and then we estimate the potential effect on the galaxy UV LF of a more gradual transition from a top-heavy IMF for Pop III stars to a standard, Salpeter-like IMF for Pop II stars, modulated by metallicity and redshift, as suggested by recent numerical simulations of star cluster formation in low-metallicity environments resolving individual forming stars (Chon & Omukai 2020; Chon et al. 2022).

4.3.1 The role of Pop III stars: CAT model prediction

CAT models stellar populations in high-redshift galaxies depending on whether their initial metallicity is smaller or larger than the critical metallicity $Z_{\rm cr}$. We therefore have an abrupt transition in the IMF, from a top-heavy IMF for Pop III stars ($Z < Z_{\rm cr}$) to a normal, Salpeter-like IMF for Pop II/I stars ($Z \geq Z_{\rm cr}$). We have shown in Fig. 6 that, according to CAT, stellar emission, including Pop III stars, cannot account for the overabundance of bright UV galaxies observed by *JWST*. To further clarify this point, in Fig. 10, we report the fraction of galaxies hosting active Pop III populations predicted by CAT at $z = 10$, 13, 15, 16, 17, and 20 (red histograms), together with the corresponding galaxy UV LF at the same redshift. At $15 \lesssim z \lesssim 20$, the fraction of galaxies hosting Pop III stars is always relatively small, and progressively shifted to fainter luminosity bins. Interestingly, however, we find that 10 per cent of some of the brightest systems at $z \sim 17$, with $M_{\rm UV} \sim -18$ host active Pop III stars. This may be ascribed to a less efficient chemical feedback at these very early times, where subsequent generations of Pop III stars form before the medium is enriched above the critical metallicity, leading to a transition in the stellar IMF. The occurrence of active Pop III stars inside bright and more massive galaxies might also be favoured by mergers with smaller metal-free DM haloes, which are supposed to occur with higher frequency at very high redshift. At $z \lesssim 16$, chemical feedback leads to a drop in the occupation fraction of active Pop III stars, especially at the bright end of the distribution. At $z \sim 15$ Pop III populations survive only in fainter and less evolved galaxies, where the gas still maintains a pristine composition. In these smaller haloes, Pop III SF is less efficient and leads preferentially to the formation of stars at the lower mass end of the Pop III IMF, which evolve on longer time-scales (see Fig. 2). Finally, below $z \sim 15$ CAT predicts a sharp transition in the brightest systems towards Pop II SF. Thereafter, Pop III stars continue to form only inside more pristine and fainter galaxies, with $M_{\rm UV} \gtrsim -10$, despite a sustained Pop III SF survives down to $z \sim 10$, where the rapid enrichment leads to a complete suppression of metal-poor SF, as shown in Fig. 3.

An important caveat of the current model is represented by the assumption of homogeneous metal enrichment and radiative feedback. Various techniques based on statistical descriptions of the DM halo distribution (Dijkstra, Ferrara & Mesinger 2014; Inayoshi et al. 2014; Salvadori et al. 2014; Sassano et al. 2021) or on *N*-body simulations to reconstruct their spatial distributions and redshift evolution (see e.g. Visbal et al. 2020; Hartwig et al. 2022; Spinoso et al. 2023; Ventura et al. 2024, for recent studies) have been developed to allow semi-analytical models to account for these spatial inhomogeneities. Our model lacks this information, although the DM halo merger trees generated with GALFORM (Parkinson et al. 2008; Trinca et al. 2022) enables us to explore different overdensities, sampling at the same time less- and more-evolved environments.

In addition, small- and large-scale gas dynamics and turbulence have been shown to be very important to allow the formation of Pop III and Pop II stellar populations in different regions of the same galaxy (Tornatore, Ferrara & Schneider 2007; Johnson, Dalla Vecchia & Khochfar 2013; Pallottini et al. 2015; Xu et al. 2016; Sarmento, Scannapieco & Côté 2019; Liu & Bromm 2020; Sarmento & Scannapieco 2022). Recent cosmological simulations by Venditti et al. (2023) show that Pop III SF might extend down to $z \sim 6$–8 in the outskirts of more metal-enriched galaxies. In particular, they predict that active Pop III stars might survive in ≥ 10 per cent of massive galaxies with $M_* \geq 3 \times 10^9\,{\rm M}_\odot$ at $z \simeq 6.7$, although with a Pop III/Pop II mass fraction $\leq$0.1 per cent. This suggests that Pop III stars formed in particularly unpolluted regions of standard main-sequence galaxies might survive below the redshift range predicted by CAT, and in a larger fraction of galaxies. However, even in this scenario, it is very unlikely that Pop III stellar systems will provide a significant contribution to the observed UV LF. The same numerical simulations show that the fraction in mass of Pop III stars inside the galaxies which mostly contribute to the $z > 10$ LF ($M_* \sim 10^8$–$10^{11}\,{\rm M}_\odot$) is between $10^{-2} - 10^{-4}$. Pop III dominated systems are expected to have fainter luminosities ($M_{\rm UV} \lesssim 11$) and lower stellar masses (see e.g. the recent observations by Vanzella et al. 2023; Maiolino et al. 2023b).

4.3.2 A more gradual transition in the stellar IMF

Recent high-resolution 3D hydrodynamical simulations of low-metallicity star-forming regions show that the metallicity-driven transition in the stellar IMF might be smoother than predicted by the critical metallicity scenario, and that a larger fraction of massive stars than predicted by a standard Salpeter-like IMF persists up to a metallicity of $Z \sim 10^{-2}\,{\rm Z}_\odot$ (Chon et al. 2021). The main effect is due

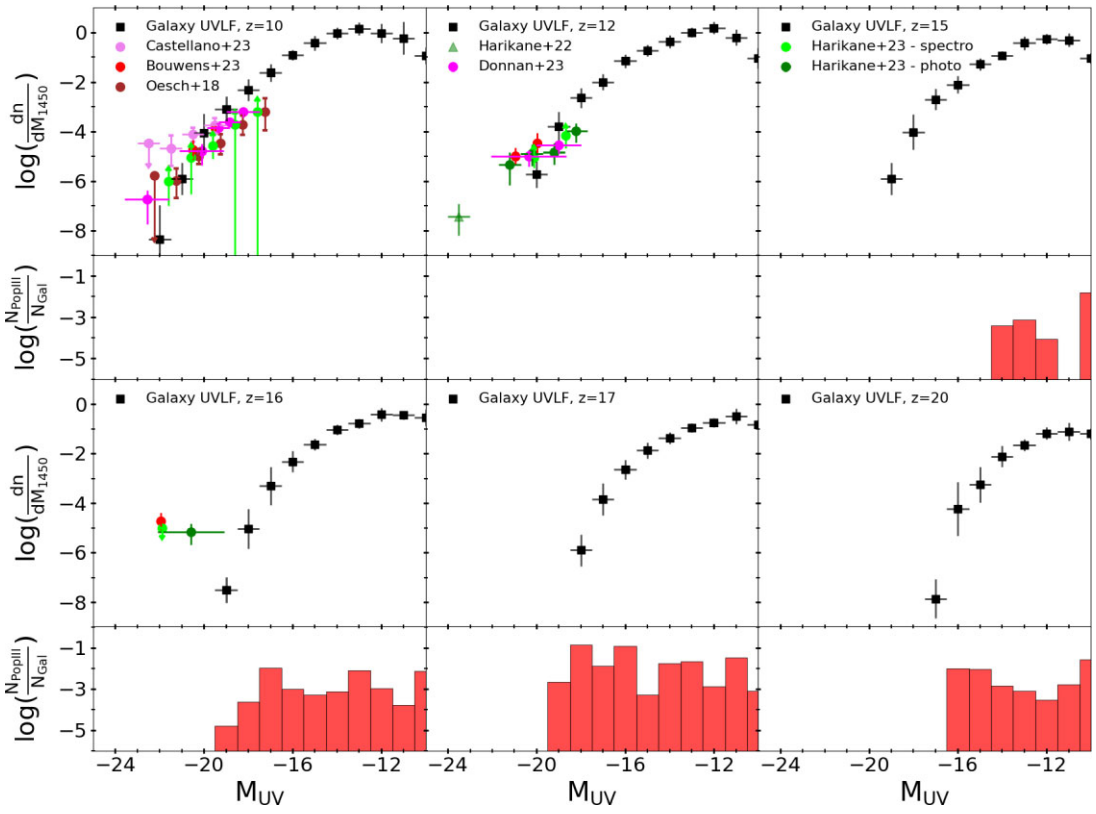

Figure 10. Galaxy UV LF predicted by CAT at $z = 10$, 13, 15, 16, 17, and 20 (from top left to bottom right). Below each panel, the red histograms show the fraction of galaxies hosting active Pop III stellar populations in each bin of magnitude. Observational data follow the same colour-coding adopted in Fig. 6.

to the interplay between the cooling time-scale and the time-scale of turbulence decay. When $Z \lesssim 10^{-2}\,Z_\odot$, SF begins after the turbulent motion decays, and a single massive cloud core monolithically collapses to form a central massive stellar cluster; despite dust-induced fragmentation occurs at $Z \geq Z_{\rm cr}$, promoting the formation of low-mass stars $m_* \lesssim 0.1$ M$_\odot$, the large gas accretion rate from the circumstellar disc preferentially feeds the central massive stars, making the mass distribution top-heavy. When $Z \geq 0.1\,Z_\odot$, efficient metal-line cooling and collisions of the turbulent flows promote the onset of SF in a highly filamentary gas structure. In this case, the mass supply to the massive stars is limited by the local gas reservoir and shared among the stars, leading to a standard Salpeter-like IMF.

In addition, the larger temperature of the CMB radiation at $z \gtrsim 10$ suppresses cloud fragmentation and reduces the number of low-mass stars in star-forming regions with metallicities $Z \gtrsim 10^{-2}\,Z_\odot$ (Schneider & Omukai 2010; Chon et al. 2022). As a result, stellar populations with metallicity of $Z \leq 10^{-2}\,Z_\odot$ or forming at $z \gtrsim 10$ are expected to be characterized by a mass spectrum consisting of a low-mass Salpeter-like component, peaking at ~ 0.1 M$_\odot$, and a top-heavy component at $\gtrsim 10$ M$_\odot$, with the mass fraction in the latter increasing with redshift, and decreasing with metallicity.

While these results rely so far only on sophisticated theoretical studies, it is tempting to investigate their potential impact on the high-z galaxy UV LF, particularly given that galaxies are expected to be more metal poor at high redshift. Indeed, galaxies observed with *JWST* at $4 < z < 9$ have been found to be relatively young, with estimated ages $t_* < 30$ Myr, and with metallicities in the range ~ 0.04–$0.7\,Z_\odot$ (see Nakajima & Maiolino 2022, and references therein), and similar properties have been derived for galaxies confirmed to be at $10 \lesssim z \lesssim 13$ (Curtis-Lake et al. 2023; Tacchella et al. 2023a, b; Bunker et al. 2023).

To quantify the effect of a redshift-modulated stellar IMF on the galaxy UV LF, here we take a simple approach and we assume that galaxies populating the bright end of the galaxy UV LF at $z \geq 10$ have metallicities $Z_* \sim 0.1\,Z_\odot$ and stellar ages $t_* \sim 10$ Myr. Following Tanikawa et al. (2022), we model the *transitional* stellar IMF as a composition of a Kroupa IMF in the mass range $0.08\,{\rm M}_\odot \leq m_* \leq 300\,{\rm M}_\odot$ (Kroupa 2001),

$$\Phi(m_*){\rm d}m_* \propto \begin{cases} m_*^{-1.3} & \text{for } 0.08\,{\rm M}_\odot \leq m_* < 0.5\,{\rm M}_\odot \\ m_*^{-2.3} & \text{for } 0.5\,{\rm M}_\odot \leq m_* \leq 300\,{\rm M}_\odot, \end{cases}$$

and of a log-flat IMF for $10\,{\rm M}_\odot \leq m_* \leq 300\,{\rm M}_\odot$,

$$\Phi(m_*)dm_* \propto m_*^{-1},$$

with a relative mass weight that depends on z and Z_* and that have been obtained by fitting the simulations results of Chon et al. (2022). For a metallicity of $Z_* = 0.1\,Z_\odot$, the weight of the log-flat IMF can be expressed as $w_{\rm LF} = 0.04 \times (z - 5)$ for $z > 5$ and it is $w_{\rm LF} = 0$ at $z \leq 5$, meaning that below this redshift all the stars follow a Kroupa IMF. Following Madau & Dickinson (2014), we use the flexible stellar population synthesis code (FSPS, Conroy, Gunn & White 2009; Conroy & Gunn 2010) to compute the conversion factor between the intrinsic specific luminosity at 1500 Å, L_ν(FUV) (expressed in units of erg s^{-1} Hz^{-1}) and the SFR (in units of M$_\odot$ yr^{-1}),

$$\mathcal{K}_{\rm FUV} = \frac{\rm SFR}{L_\nu({\rm FUV})}, \tag{17}$$

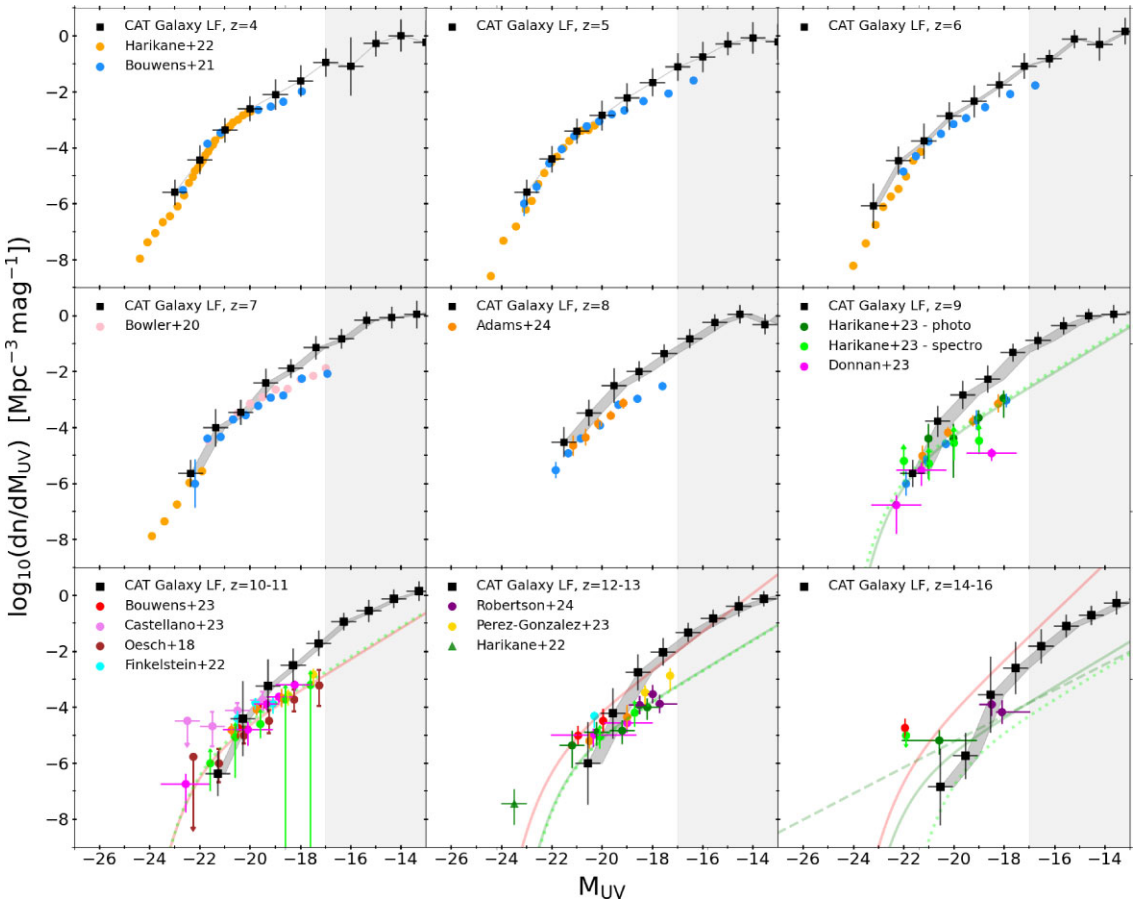

Figure 11. Galaxy UV LF, as in Fig. 6, but assuming the $\mathcal{K}_{\rm FUV}$ expected for a stellar population of 10 Myr with a transitional IMF, as described in the text. Black-shaded regions show how the predicted LFs are shifted towards higher luminosities with respect to the previous distribution. Observational data follow the same colour-coding adopted in Fig. 6.

assuming a constant SFR and our adopted transitional stellar IMF for $Z_* = 0.1\ {\rm Z}_\odot$. At redshift $z = (0 - 5, 10, 15, 20)$, we find that $\mathcal{K}_{\rm FUV} = (1.46, 1.21, 1.04, 0.91) \times 10^{-28}$ for a stellar age of $t_* = 10$ Myr, and $\mathcal{K}_{\rm FUV} = (1.12, 0.96, 0.90, 0.81) \times 10^{-28}$ for $t_* = 20$ Myr. Hence, a stellar population with the same metallicity and age is predicted to emit up to 1.4–1.8 times more FUV radiation per unit SFR at $z \sim 20$ than at $z \lesssim 10$.

In Fig. 11, we show how the predicted galaxy UV LF changes when applying to the Pop II stellar emission a correction for $\mathcal{K}_{\rm FUV}$ consistent with a stellar population characterized by a composite IMF. We assume a boost in the luminosity of each galaxy of a factor $\mathcal{K}_{\rm FUV}(z)/\mathcal{K}_{\rm FUV,Kroupa}$, where $\mathcal{K}_{\rm FUV,Kroupa} = 1.46 \times 10^{-28}$ and $\mathcal{K}_{\rm FUV}(z)$ are the expected correction factors for, respectively, the Kroupa and the composite IMFs, assuming a stellar population of 10 Myr with $Z_* = 0.1\ {\rm Z}_\odot$. We see how this correction impacts significantly on the UV LF, especially at $z \gtrsim 9$. In particular, CAT predictions are now consistent with observational constraints in the redshift ranges $z \sim$ 10–11 and $\sim$ 12–13. At $z \sim$ 14–16, the model predicts number density of UV bright sources that is still smaller than estimated from photometric candidates (Harikane et al. 2024) and consistent with the lower limit inferred from the spectroscopic analysis (Harikane et al. 2024), but the difference from their best-fitting model is now reduced to 0.5 and 0.8 dex at, respectively, $M_{\rm UV} \simeq -19.5$ and $\simeq -20.5$ (see Fig. 12).

Hence, by considering a gradual transition in the stellar IMF modulated by metallicity and redshift, we are able to recover a better match with the observational estimates of the number density of bright sources at $z \gtrsim 10$. A minor discrepancy persists in the highest redshift range, $z > 14$, where the model predictions are also affected by large statistical uncertainties. In a future study, we plan to incorporate these new theoretical findings into a more sophisticated modelling of stellar populations in CAT, as a transitional IMF that depends on metallicity and redshift not only affect the emissivity of the first galaxies, but it also changes the rate of SN explosion, hence the effects of mechanical and chemical feedback. In addition, it modifies the mass function of BH remnants, with interesting consequences on the BH seed populations.

4.4 Quantifying the tension with *JWST* data

We quantify the tension between the predictions of the model that we have explored with current observations in Fig. 12, where we compare the number density of galaxies with $M_{\rm UV} \sim -20$ predicted by CAT (coloured histograms) in the redshift range $z \sim$ 10–11 (left panel), $z \sim$ 12–13 (middle panel), and $z \sim$ 14–16 (right panel), with the observational estimates of Bouwens et al. (2023, horizontal red line) and Harikane et al. (2023b, horizontal green line), based on photometric candidates, and with analysis of Harikane et al. (2024, horizontal light green), based on spectroscopically confirmed

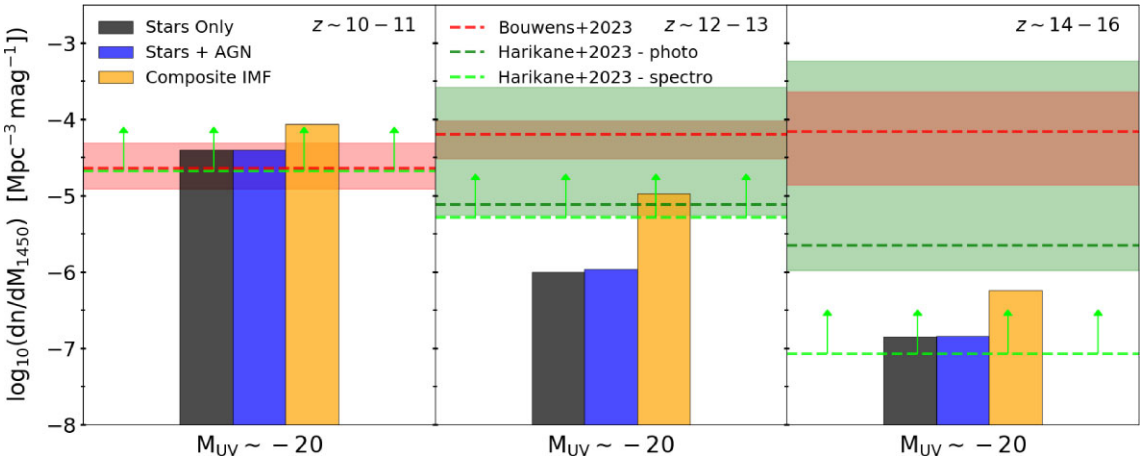

Figure 12. CAT prediction for the number density of galaxies with $M_{UV} \sim -20$ in the redshift range $z \sim 10$–11, ~ 12–13, and ~ 14–16. The different coloured histograms show the obtained values for the stellar-only galaxy LF (black bars), the total UV LF (stars + AGN, blue bars), and the galaxy LF corrected for a composite stellar IMF (orange bars). The horizontal lines represent the empirical estimates obtained from the best-fitting LFs of Harikane et al. (2023b, dark green) and Bouwens et al. (2023, red), with the shaded regions showing the $1\,\sigma$ error. The light green horizontal lines show instead the estimates based only on spectroscopically confirmed galaxies obtained by Harikane et al. (2024), which are represented here as lower limit of the galaxy number density.

galaxies. The values obtained from the photometric samples have been estimated from the Schechter fits[4] of the LF at $M_{UV} \simeq -20$ reported in the original papers, with their associated errors. The value estimated from the spectroscopic sample is reported as a lower limit. The three coloured histograms represent the number density of sources predicted by CAT when the UV luminosity is computed according to CAT reference model considering only the emission from stars (black) and from stars and accreting BHs (blue), while the orange histograms show the result of computing the stellar emission according to a transitional IMF. As anticipated, considering the AGN contribution in addition to the stellar emission does not significantly increase the number density of sources with $M_{UV} \simeq -20$ at $z \gtrsim 10$. CAT reference model predictions are consistent with observations at $z \simeq 10$–11, but fall short by 0.8 dex at $z \simeq 12$–13, and 1.2 dex at $z \sim 14$–16, compared to the values estimated by Harikane et al. (2023b), and by 1.8 dex at $z \simeq 12$–13, and 2.7 dex at $z \sim 14$–16, compared to the values estimated by Bouwens et al. (2023), while being consistent with the lower limit estimated by Harikane et al. (2024) at $z \sim 14$–16. Interestingly, the increase in the UV luminosity predicted by a transitional IMF brings the model in agreement with the observational estimate at $z \sim 12$–13 by Harikane et al. (2023b), and reduces the disagreement with their best-fitting value to 0.6 dex at $z \sim 14$–16, while the estimated values from Bouwens et al. (2023) are still 0.8 dex (2.1 dex) higher than the model predictions at $z \sim 12$–13 ($z \sim 14$–16).

5 CONCLUSIONS

In this study, we have explored the contribution of Pop III/II stars and accreting BH seeds to the UV luminosity evolution at $4 \leq z \leq 20$ using the CAT model. We first presented the predictions of CAT regarding the cosmic SF history and the contributions of the first galaxies and their nuclear BHs to cosmic reionization. We then compared the galaxy UV LF at $4 \leq z \leq 20$ with available observations, from deep *HST* and *JWST* data, discussing the contribution of emission from stars, including Pop III stars, and accreting BHs. We find that:

(i) The model predicts a cosmic SF history dominated by UV faint ($M_{UV} > -18$) galaxies populated by Pop II/I stars. In the redshift range $4 < z < 10$, CAT predictions for the total SFRD are in very good agreement with data inferred from gamma-ray burst observations, which are sensitive to both obscured and unobscured SF (Kistler et al. 2009; Robertson & Ellis 2012). Conversely, the SFRD derived from the rest-frame UV luminosity are better reproduced by CAT when only the contribution of the sources brightest than $M_{UV} \simeq -18$ is considered (Trinca et al. 2022).

(ii) At $10 \lesssim z \lesssim 20$, the formation of Pop III stars is strongly self-regulated, their SFRD remains almost constant, and their contribution to the total SFRD ranges from $\lesssim 10$ per cent down to $\lesssim 0.5$ per cent. Below $z \sim 10$, chemical feedback prevents further episodes of Pop III SF.

(iii) CAT predicts a cosmic reionization process consistent with current observational constraints. Stars are the primary sources of cosmic reionization, with 5 per cent − 10 per cent of ionizing photons escaping into the IGM at $5 \leq z \leq 10$, in good agreement with recent results (Schaerer 2002; Finkelstein et al. 2019; Naidu et al. 2020; Mascia et al. 2023). Due to their top-heavy IMF and lower metallicity, Pop III stars dominate the emissivity down to $z \simeq 16$. The AGN ionizing emissivity remains subdominant with respect to the Pop II stellar emission down to $z \sim 5$.

Having satisfied these global constraints, we have investigated the redshift evolution of the galaxy UV LF predicted by CAT, comparing it with deep *HST* data and with recent *JWST* observations. We find that:

(i) The stellar and AGN UV LFs predicted by CAT are in good agreement with observations at $5 \lesssim z \lesssim 9$–10. At higher redshift, CAT predicts a steeper faint-end slope than the observed best-fitting LFs extrapolated at $M_{UV} > -18$, suggesting that stars may form too efficiently, feedback may be too inefficient, or that current observational samples may be still incomplete at these faint luminosities.

[4]In general, the LF are best fit assuming both a double-power-law and a Schechter function, but due to the uncertainties in the measurements, the difference between the two is small at $z \sim 9$, and negligible at $z \sim 12$ and 16 Harikane et al. (2023b).

(ii) When considering only the emission from stars, the UV LF predicted by CAT at the bright end shows a mild evolution at $10 \lesssim z \lesssim 13$, consistent with observations, except for the highest luminosity bins, at $M_{\rm UV} < -19$, where the model seems to underestimate the number of bright objects, despite the large statistical uncertainties. We quantified this tension by comparing the number density of $M_{\rm UV} \sim -20$ galaxies with recent *JWST* data, finding that the model predictions are consistent with observations at $z \simeq 10$–11, but fall short by 0.8 dex at $z \simeq 12$–13, and 1.2 dex at $z \sim 14$–16, compared to the values estimated by Harikane et al. (2023b), and by 1.8 dex at $z \simeq 12$–13, and 2.7 dex at $z \sim 14$–16, compared to the values estimated by Bouwens et al. (2023), while being consistent with the lower limit estimated by Harikane et al. (2024) at $z \sim 14$–16.

(iii) Including the emission by AGNs does not affect these findings. In fact, at $z \gtrsim 15$, the AGN emission appears negligible, due to the stunted growth of light seeds predicted by our reference model (see Trinca et al. 2022). At $10 \lesssim z \lesssim 15$, during the formation epoch of heavy BH seeds, the AGN emission contributes on average to ~ 1–3 per cent of the total UV emission, and their largest contamination reaches $\lesssim 10$ per cent in the brightest bins of magnitude, at $M_{\rm UV} \lesssim -19$. However, the AGN emission becomes progressively more important at lower redshift, with an average (maximum) contribution of $\lesssim 20$ per cent (> 50 per cent) at $7 \lesssim z \lesssim 10$, and of 20 per cent $-$ 100 per cent at $z < 7$ in systems with $M_{\rm UV} \lesssim -22$.

(iv) Metal-free and very metal-poor stellar populations might also increase the UV luminosity of galaxies at $z \gtrsim 10$. Our results suggest that Pop III stars, with their harder emission spectra, contribute to the UV luminosity in up to ~ 10 per cent of high-redshift systems at $z \gtrsim 16$, while their contribution becomes significantly smaller with decreasing redshift, due to the progression of metal enrichment.

(v) Finally, we have explored the effects on the UV luminosities of a more gradual transition in the stellar IMF, as suggested by recent high-resolution numerical simulations (Chon et al. 2021,2022). We model this transitional IMF as a superposition of a Kroupa and a log-flat IMF, with a relative weight that depends both on redshift and on the initial stellar metallicity, Z_*. Assuming a fixed value of $Z_* = 0.1\ {\rm Z}_\odot$ and a constant stellar age of $t_* = 10$ Myr, we find that galaxies emit 30 per cent more UV photons per unit SFR at $z \simeq 10$ and 60 per cent at $z \simeq 20$ than at $z \lesssim 5$, where a standard Kroupa IMF applies. When accounting for this effect, the number density of $M_{\rm UV} \sim -20$ galaxies predicted by the model is in agreement with the observational estimate at $z \sim 12$–13 by Harikane et al. (2023b), and reduces the disagreement with their best-fitting value to 0.6 dex at $z \sim 14$–16, while the estimated values from Bouwens et al. (2023) are still 0.8 dex (2.1 dex) higher than the model predictions at $z \sim 12$–13 ($z \sim 14$–16).

If the current tension between theoretical models and *JWST* observations will consolidate on the basis of a larger sample of spectroscopically confirmed galaxies at $z \gtrsim 10$, this opens up the prospective of exploring the nature of the first sources that inhabit early galaxies, and to improve our understanding of the physical processes that shape the assembly of cosmic structures at these remote cosmic epochs.

ACKNOWLEDGEMENTS

We acknowledge support from the PRIN 2022 MUR project 2022CB3PJ3 – First Light And Galaxy aSsembly (FLAGS) funded by the European Union – Next Generation EU, from the Amaldi Research Center funded by the MIUR program 'Dipartimento di Eccellenza' (CUP:B81I18001170001), and from the INFN TEONGRAV specific initiative. This research is supported in part by grants-in-aid for Scientific Research (KO: 17H06360, 17H01102, 17H02869, and 22H00149) from the Japan Society for the Promotion of Science. AT and RV acknowledge support from the PRIN 2022 MUR project 2022935STW and 2023 INAF Theory Grant "Theoretical models for Black Holes Archaeology"

DATA AVAILABILITY

The simulated data underlying this article will be shared on reasonable request to the corresponding author.

REFERENCES

Adams N. J. et al., 2023a, preprint (arXiv:2304.13721)
Adams N. J. et al., 2023b, MNRAS, 518, 4755
Aguado D. S. et al., 2023, A&A, 669, L4
Algera H. S. B. et al., 2023, MNRAS, 518, 6142
Arrabal Haro P. et al., 2023, Nature, 622, 707
Atek H. et al., 2023, MNRAS, 519, 1201
Backhaus B. E. et al., 2022, ApJ, 926, 161
Baldwin J. A., Phillips M. M., Terlevich R., 1981, PASP, 93, 5
Barkana R., Loeb A., 2001, Phys. Rep., 349, 125
Barrufet L. et al., 2023, MNRAS, 522, 449
Becerra F., Greif T. H., Springel V., Hernquist L. E., 2015, MNRAS, 446, 2380
Becerra F., Marinacci F., Bromm V., Hernquist L. E., 2018, MNRAS, 480, 5029
Becker G. D., Bolton J. S., 2013, MNRAS, 436, 1023
Becker G. D., D'Aloisio A., Christenson H. M., Zhu Y., Worseck G., Bolton J. S., 2021, MNRAS, 508, 1853
Behroozi P., Wechsler R. H., Hearin A. P., Conroy C., 2019, MNRAS, 488, 3143
Bolan P. et al., 2022, MNRAS, 517, 3263
Bondi H., 1952, MNRAS, 112, 195
Bouwens R. J. et al., 2012, ApJ, 754, 83
Bouwens R. J. et al., 2014, ApJ, 795, 126
Bouwens R. J. et al., 2021, AJ, 162, 47
Bouwens R., Illingworth G., Oesch P., Stefanon M., Naidu R., van Leeuwen I., Magee D., 2023, MNRAS, 523, 1009
Bowler R. A. A., Jarvis M. J., Dunlop J. S., McLure R. J., McLeod D. J., Adams N. J., Milvang-Jensen B., McCracken H. J., 2020, MNRAS, 493, 2059
Bradley L. D. et al., 2023, ApJ, 955, 13
Bromm V., Kudritzki R. P., Loeb A., 2001, ApJ, 552, 464
Bruzual G., Charlot S., 2003, MNRAS, 344, 1000
Bunker A. J. et al., 2023, A&A, 677, A88
Castellano M. et al., 2022, ApJ, 938, L15
Castellano M. et al., 2023, ApJ, 948, L14
Chon S., Hosokawa T., Omukai K., 2021, MNRAS, 502, 700
Chon S., Omukai K., 2020, MNRAS, 494, 2851
Chon S., Ono H., Omukai K., Schneider R., 2022, MNRAS, 514, 4639
Cleri N. J. et al., 2023, ApJ, 953, 10
Conroy C., Gunn J. E., 2010, ApJ, 712, 833
Conroy C., Gunn J. E., White M., 2009, ApJ, 699, 486
Curti M. et al., 2023, MNRAS, 518, 425
Curtis-Lake E. et al., 2023, Nat. Astron., 7, 622
Davies F. B. et al., 2018, ApJ, 864, 142
Dayal P. et al., 2020, MNRAS, 495, 3065
de Bennassuti M., Salvadori S., Schneider R., Valiante R., Omukai K., 2017, MNRAS, 465, 926
de Bennassuti M., Schneider R., Valiante R., Salvadori S., 2014, MNRAS, 445, 3039
Dekel A., Sarkar K. S., Birnboim Y., Mandelker N., Li Z., 2023, MNRAS, 523, 3201

Dijkstra M., Ferrara A., Mesinger A., 2014, MNRAS, 442, 2036
Donnan C. T. et al., 2023, MNRAS, 518, 6011
Dubois Y., Volonteri M., Silk J., 2014, MNRAS, 440, 1590
Duras F. et al., 2020, A&A, 636, A73
Ellis R. S. et al., 2013, ApJ, 763, L7
Ferrara A., Pallottini A., Dayal P., 2023, MNRAS, 522, 3986
Ferrara A., Salvadori S., Yue B., Schleicher D., 2014, MNRAS, 443, 2410
Fialkov A., Barkana R., Visbal E., Tseliakhovich D., Hirata C. M., 2013, MNRAS, 432, 2909
Finkelstein S. L. et al., 2019, ApJ, 879, 36
Finkelstein S. L. et al., 2022, ApJ, 940, L55
Finkelstein S. L. et al., 2023, ApJ, 946, L13
Finkelstein S. L., Bagley M. B., 2022, ApJ, 938, 25
Fiore F., Ferrara A., Bischetti M., Feruglio C., Travascio A., 2023, ApJ, 943, L27
Fraser M., Casey A. R., Gilmore G., Heger A., Chan C., 2017, MNRAS, 468, 418
Furtak L. J., Shuntov M., Atek H., Zitrin A., Richard J., Lehnert M. D., Chevallard J., 2023, MNRAS, 519, 3064
Ganguly R., Brotherton M. S., Cales S., Scoggins B., Shang Z., Vestergaard M., 2007, ApJ, 665, 990
Giallongo E. et al., 2019, ApJ, 884, 19
Goulding A. D., Greene J. E., 2022, ApJ, 938, L9
Greene J. E. et al., 2023, preprint (arXiv:2309.05714)
Greig B., Mesinger A., Bañados E., 2019, MNRAS, 484, 5094
Gruppioni C. et al., 2020, A&A, 643, A8
Harikane Y. et al., 2022a, ApJS, 259, 20
Harikane Y. et al., 2022b, ApJ, 929, 1
Harikane Y. et al., 2023a, ApJ, 959, 39
Harikane Y. et al., 2023b, ApJS, 265, 5
Harikane Y., Nakajima K., Ouchi M., Umeda H., Isobe Y., Ono Y., Xu Y., Zhang Y., 2024, ApJ, 960, 56
Hartwig T. et al., 2022, ApJ, 936, 45
Heintz K. E. et al., 2023a, Nat. Astron., 7, 1517
Heintz K. E. et al., 2023b, ApJ, 944, L30
Hirano S., Hosokawa T., Yoshida N., Umeda H., Omukai K., Chiaki G., Yorke H. W., 2014, ApJ, 781, 60
Hirano S., Zhu N., Yoshida N., Spergel D., Yorke H. W., 2015, ApJ, 814, 18
Hosokawa T., Hirano S., Kuiper R., Yorke H. W., Omukai K., Yoshida N., 2016, ApJ, 824, 119
Hosokawa T., Omukai K., Yorke H. W., 2012, ApJ, 756, 93
Hosokawa T., Omukai K., Yoshida N., Yorke H. W., 2011, Science, 334, 1250
Hoyle F., Lyttleton R. A., 1941, MNRAS, 101, 227
Iliev I. T., Scannapieco E., Shapiro P. R., 2005, ApJ, 624, 491
Inayoshi K., Omukai K., Tasker E., 2014, MNRAS, 445, L109
Inayoshi K., Onoue M., Sugahara Y., Inoue A. K., Ho L. C., 2022, ApJ, 931, L25
Inayoshi K., Visbal E., Haiman Z., 2020, ARA&A, 58, 27
Ishiyama T. et al., 2021, MNRAS, 506, 4210
Jaacks J., Finkelstein S. L., Bromm V., 2019, MNRAS, 488, 2202
Johnson J. L., Dalla Vecchia C., Khochfar S., 2013, MNRAS, 428, 1857
Katz H., Kimm T., Ellis R. S., Devriendt J., Slyz A., 2023, MNRAS, 524, 351
Keller B. W., Munshi F., Trebitsch M., Tremmel M., 2023, ApJ, 943, L28
Khusanova Y. et al., 2021, A&A, 649, A152
Kistler M. D., Yüksel H., Beacom J. F., Hopkins A. M., Wyithe J. S. B., 2009, ApJ, 705, L104
Kocevski D. D. et al., 2023, ApJ, 954, L4
Kroupa P., 2001, MNRAS, 322, 231
Kuhlen M., Faucher-Giguère C.-A., 2012, MNRAS, 423, 862
Labbe I. et al., 2023, Nature, 616, 266
Larson R. L. et al., 2023, ApJ, 953, L29
Latif M. A., Ferrara A., 2016, Publ. Astron. Soc. Aust., 33, e051
Latif M. A., Schleicher D. R. G., Schmidt W., Niemeyer J. C., 2013, MNRAS, 436, 2989
Liu B., Bromm V., 2020, MNRAS, 497, 2839
Madau P., Dickinson M., 2014, ARA&A, 52, 415
Madau P., Haardt F., Dotti M., 2014, ApJ, 784, L38
Magg M., Schauer A. T. P., Klessen R. S., Glover S. C. O., Tress R. G., Jaura O., 2022, ApJ, 929, 119
Maio U., Petkova M., De Lucia G., Borgani S., 2016, MNRAS, 460, 3733
Maiolino R. et al., 2024, Nature, 627, 59, available at:
Maiolino R. et al., 2023b, preprint (arXiv:2306.00953)
Maiolino R. et al., 2023c, preprint (arXiv:2308.01230)
Mancini M., Schneider R., Graziani L., Valiante R., Dayal P., Maio U., Ciardi B., 2016, MNRAS, 462, 3130
Mascia S. et al., 2023, A&A, 672, A155
Mason C. A., Trenti M., Treu T., 2023, MNRAS, 521, 497
Matthee J. et al., 2024, ApJ 963 129
McCaffrey J., Hardin S., Wise J., Regan J., 2023, Open J. Astrophys., 6, 47
McGreer I. D., Fan X., Jiang L., Cai Z., 2018, AJ, 155, 131
McGreer I. D., Mesinger A., D'Odorico V., 2015, MNRAS, 447, 499
McLeod D. J. et al., 2024, MNRAS, 527, 5004
Menci N., Castellano M., Santini P., Merlin E., Fontana A., Shankar F., 2022, ApJ, 938, L5
Merlin E. et al., 2019, MNRAS, 490, 3309
Mirocha J., Furlanetto S. R., 2023, MNRAS, 519, 843
Mo H. J., Mao S., White S. D. M., 1998, MNRAS, 295, 319
Morales A. M., Mason C. A., Bruton S., Gronke M., Haardt F., Scarlata C., 2021, ApJ, 919, 120
Naidu R. P. et al., 2022, ApJ, 940, L14
Naidu R. P., Tacchella S., Mason C. A., Bose S., Oesch P. A., Conroy C., 2020, ApJ, 892, 109
Nakajima K., Maiolino R., 2022, MNRAS, 513, 5134
Natarajan P., Pacucci F., Ferrara A., Agarwal B., Ricarte A., Zackrisson E., Cappelluti N., 2017, ApJ, 838, 117
Negri A., Volonteri M., 2017, MNRAS, 467, 3475
Niida M. et al., 2020, ApJ, 904, 89
Oesch P. A., Bouwens R. J., Illingworth G. D., Labbé I., Stefanon M., 2018, ApJ, 855, 105
Omukai K., Nishi R., 1998, ApJ, 508, 141
Omukai K., Palla F., 2003, ApJ, 589, 677
Omukai K., Tsuribe T., Schneider R., Ferrara A., 2005, ApJ, 626, 627
Pacucci F., Dayal P., Harikane Y., Inoue A. K., Loeb A., 2022, MNRAS, 514, L6
Pacucci F., Loeb A., 2020, ApJ, 895, 95
Pallottini A. et al., 2015, MNRAS, 453, 2465
Parkinson H., Cole S., Helly J., 2008, MNRAS, 383, 557
Parsa S., Dunlop J. S., McLure R. J., 2018, MNRAS, 474, 2904
Pérez-González P. G. et al., 2023, ApJ, 951, L1
Pfister H., Volonteri M., Dubois Y., Dotti M., Colpi M., 2019, MNRAS, 486, 101
Piana O., Dayal P., Choudhury T. R., 2022, MNRAS, 510, 5661
Planck Collaboration VI, 2020, A&A, 641, A6
Planck Collaboration XIII, 2016, A&A, 594, A13
Prada F., Behroozi P., Ishiyama T., Klypin A., Pérez E., 2023, preprint (arXiv:2304.11911)
Reines A. E., Volonteri M., 2015, ApJ, 813, 82
Ricci F., Marchesi S., Shankar F., La Franca F., Civano F., 2017, MNRAS, 465, 1915
Robertson B. E. et al., 2023, Nat. Astron., 7, 611
Robertson B. E., Ellis R. S., 2012, ApJ, 744, 95
Salvadori S., Tolstoy E., Ferrara A., Zaroubi S., 2014, MNRAS, 437, L26
Sarmento R., Scannapieco E., 2022, ApJ, 935, 174
Sarmento R., Scannapieco E., Côté B., 2019, ApJ, 871, 206
Sassano F., Capelo P. R., Mayer L., Schneider R., Valiante R., 2023, MNRAS, 519, 1837
Sassano F., Schneider R., Valiante R., Inayoshi K., Chon S., Omukai K., Mayer L., Capelo P. R., 2021, MNRAS, 506, 613
Schaerer D., 2002, A&A, 382, 28
Schaerer D., Marques-Chaves R., Barrufet L., Oesch P., Izotov Y. I., Naidu R., Guseva N. G., Brammer G., 2022, A&A, 665, L4
Schenker M. A. et al., 2013, ApJ, 768, 196
Schneider R., Omukai K., 2010, MNRAS, 402, 429
Schneider R., Valiante R., Trinca A., Graziani L., Volonteri M., Maiolino R., 2023, MNRAS, 526, 3250

Shakura N. I., Sunyaev R. A., 1973, A&A, 500, 33
Skinner D., Wise J. H., 2020, MNRAS, 492, 4386
Spinoso D., Bonoli S., Valiante R., Schneider R., Izquierdo-Villalba D., 2023, MNRAS, 518, 4672
Sugimura K., Matsumoto T., Hosokawa T., Hirano S., Omukai K., 2020, ApJ, 892, L14
Sugimura K., Omukai K., Inoue A. K., 2014, MNRAS, 445, 544
Susa H., Hasegawa K., Tominaga N., 2014, ApJ, 792, 32
Tacchella S. et al., 2023a, MNRAS, 522, 6236
Tacchella S. et al., 2023b, ApJ, 952, 74
Tanaka T., Haiman Z., 2009, ApJ, 696, 1798
Tanikawa A., Yoshida T., Kinugawa T., Trani A. A., Hosokawa T., Susa H., Omukai K., 2022, ApJ, 926, 83
Tornatore L., Ferrara A., Schneider R., 2007, MNRAS, 382, 945
Tremmel M. et al., 2019, MNRAS, 483, 3336
Tremmel M., Governato F., Volonteri M., Quinn T. R., Pontzen A., 2018, MNRAS, 475, 4967
Trinca A., Schneider R., Maiolino R., Valiante R., Graziani L., Volonteri M., 2023, MNRAS, 519, 4753
Trinca A., Schneider R., Valiante R., Graziani L., Zappacosta L., Shankar F., 2022, MNRAS, 511, 616
Trussler J. A. A., Conselice C. J., Adams N. J., Maiolino R., Nakajima K., Zackrisson E., Ferreira L., 2023, MNRAS, 525, 5328
Übler H. et al., 2023, A&A, 677, A145
Ueda Y., Akiyama M., Hasinger G., Miyaji T., Watson M. G., 2014, ApJ, 786, 104
Valiante R., Schneider R., Salvadori S., Bianchi S., 2011, MNRAS, 416, 1916
Valiante R., Schneider R., Salvadori S., Gallerani S., 2014, MNRAS, 444, 2442
Valiante R., Schneider R., Volonteri M., Omukai K., 2016, MNRAS, 457, 3356
Valiante R., Schneider R., Zappacosta L., Graziani L., Pezzulli E., Volonteri M., 2018, MNRAS, 476, 407
Vanzella E. et al., 2023, ApJ, 945, 53
Venditti A., Graziani L., Schneider R., Pentericci L., Di Cesare C., Maio U., Omukai K., 2023, MNRAS, 522, 3809
Ventura E. M., Qin Y., Balu S., Wyithe J. S. B., 2024, MNRAS, 529, 628, available at:
Visbal E., Bryan G. L., Haiman Z., 2020, ApJ, 897, 95
Volonteri M. et al., 2020, MNRAS, 498, 2219
Volonteri M., Habouzit M., Colpi M., 2023, MNRAS, 521, 241
Wang F. et al., 2020, ApJ, 896, 23
Wang X. et al., 2022, preprint (arXiv:2212.04476)
Weinberger R. et al., 2017, MNRAS, 465, 3291
Weingartner J. C., Draine B. T., 2001, ApJ, 548, 296
Welch B. et al., 2022, ApJ, 940, L1
Williams H. et al., 2023, Science, 380, 416
Wolcott-Green J., Haiman Z., Bryan G. L., 2017, MNRAS, 469, 3329
Woods T. E. et al., 2019, PASA, 36, e027
Xu H., Norman M. L., O'Shea B. W., Wise J. H., 2016, ApJ, 823, 140
Yoshida N., Omukai K., Hernquist L., 2008, Science, 321, 669
Yung L. Y. A., Somerville R. S., Finkelstein S. L., Wilkins S. M., Gardner J. P., 2024, MNRAS, 527, 5929
Zavala J. A. et al., 2023, ApJ, 943, L9
Zhang H., Behroozi P., Volonteri M., Silk J., Fan X., Hopkins P. F., Yang J., Aird J., 2023, MNRAS, 518, 2123
Ziparo F., Ferrara A., Sommovigo L., Kohandel M., 2023, MNRAS, 520, 2445

This paper has been typeset from a TEX/LATEX file prepared by the author.